Microporous and Mesoporous Materials 270 (2018) 10–23

Contents lists available at ScienceDirect

Microporous and Mesoporous Materials

journal homepage: www.elsevier.com/locate/micromeso

Synthetic strategies for the encapsulation of nanoparticles of Ni, Co, and Fe oxides within crystalline microporous aluminosilicates

Trenton Otto[a], Stacey I. Zones[b], Enrique Iglesia[a,c,*]

[a] Department of Chemical and Biomolecular Engineering, University of California at Berkeley, Berkeley, CA 94720, USA
[b] Chevron Energy Technology Company, Richmond, CA 94804, USA
[c] Division of Chemical Sciences, E.O. Lawrence Berkeley National Laboratory, Berkeley, CA 94720, USA

ARTICLE INFO

Keywords:
Zeolite encapsulation
Metal oxide nanoparticles
Hydrothermal synthesis
Size-selective catalysis

ABSTRACT

A synthetic strategy is reported here for the selective containment of oxide nanoparticles of base metals within zeolitic voids of molecular dimensions. The technique, though generally applicable, is specifically illustrated to encapsulate Ni, Co, and Fe oxides within LTA, MFI, and FAU zeolites through hydrothermal framework crystallization in the presence of ligand-protected metal cations. Such ligands contain bidentate amine groups that preclude the precipitation of metal precursors in alkaline synthesis gels, and alkoxysilane moieties that form covalent linkages with nucleating zeolite precursors to enforce metal uptake into crystallized solids. These ligands are removed by subsequent oxidative treatments that nucleate oxide nanoparticles without structural degradation of the zeolites. The clusters are small (< 2.5 nm) and uniformly distributed in size, reflecting their constrained growth within zeolite crystals. In contrast with exchange strategies for encapsulation, which lead to grafted cations and dense metal aluminosilicates, these methods form oxide nanoparticles, evident from infrared spectra of samples exposed to CO. Oxide nanoparticles undergo more facile redox cycles than grafted cations or dense aluminosilicates, thus rendering oxide domains more effective oxidation catalysts. The dynamics and stoichiometry of nanoparticle reduction in H_2 confirmed the presence of NiO, Co_3O_4, and Fe_2O_3 clusters and their more facile reducibility relative to metal aluminosilicates. Ethanol oxidation rates on these clusters were essentially unaffected by exposure to bulky thiol poisons that titrate metal oxide surfaces, reflecting the selective placement of the oxide nanoparticles within the confines of microporous voids, where they are protected from contact by large molecules. These synthetic strategies and guiding principles circumvent long-standing hurdles in the selective encapsulation of base metals, and provide enabling routes for the synthesis of the many metal-zeolite systems that confront similar hurdles.

1. Introduction

Crystalline microporous solids, such as zeotypes, are ubiquitous in water purification [1], molecular separations [2], and catalysis [3,4]. Their applications exploit the molecular sieving and shape-selective properties of zeotypes, which lead to preferential access to intracrystalline regions by specific molecules, based on the size and shape of the connecting apertures and cavities within each porous framework [2,5]. Zeolite catalysts, in particular, benefit from the exclusion of large reactive or poison molecules from intracrystalline active sites [5], from the retention of large products until they fragment and egress more readily as smaller species [6], and from the preferential stabilization of specific transition states within intracrystalline voids [7]. These properties can be combined with the inherent catalytic properties of metal surfaces by encapsulating clusters of metals within zeolite voids and, in doing so, synthesizing size-selective and shape-selective metal catalysts [8–10]. Such clusters benefit from significant resistance to coalescence as a consequence of confinement, thus allowing them to retain their small dimensions under conditions that would cause their significant coalescence and sintering when dispersed on mesoporous supports [8–11].

Most noble metals, including Pt, Pd, Ir, Re, Rh, Ag, Au [8,11], and their bimetallic mixtures [9,12] have been successfully encapsulated within several zeolites (e.g., CHA [13], LTA [11], MFI [8,14], FAU [12,15]). Ion exchange of metal cations and their subsequent reduction by H_2 enable encapsulation of these metals within large-pore zeolites (12-member ring (MR) apertures or larger; e.g., FAU) [15]. Such methods become unsuitable for small-pore (8 MR) zeolites and, in some cases, for medium-pore (10 MR) zeolites, because of the slow diffusion of solvated aqueous precursors through their narrow apertures [16]. In

---

[*] Corresponding author. University of California, 103 Gilman Hall, Berkeley, CA 94720-1462, USA.
E-mail address: iglesia@berkeley.edu (E. Iglesia).

https://doi.org/10.1016/j.micromeso.2018.04.045
Received 3 March 2018; Received in revised form 3 April 2018; Accepted 27 April 2018

such instances, encapsulation requires the hydrothermal crystallization of zeolite frameworks around solvated precursors, which must be stabilized by ligands against precipitation or reduction at the pH and temperatures of crystallization [8,11]. Such ligands are subsequently removed by thermal treatments in oxidative or reductive environments to form stable and catalytically-competent encapsulated metal clusters [8,11].

The encapsulation of clusters of base metals (e.g., Ni, Co, and Fe) and their oxides [10] is also of significant interest because of their ubiquitous use as catalysts. NiO, Co_3O_4, and Fe_2O_3 are effective oxidation catalysts for diverse substrates, such as CO [17–19], alcohols [20–22], and methane [23]. These oxides can be reduced to their metallic state in order to render them useful as catalysts for hydrocarbon reforming (Ni) [24], aldehyde hydrogenation (Ni) [25], Fischer-Tropsch synthesis (Co, Fe) [26], and ammonia synthesis (Fe) [27]. Ni^{2+}, Co^{2+}, and Fe^{2+} cations can be exchanged from aqueous media onto most zeolites because they can diffuse (along with their double-layer) in their divalent state even through 8-MR zeolite apertures [28,29]. The conversion of these exchanged cations into metal clusters through post-exchange reductive treatments in H_2 or CO, however, cannot be used in general to form encapsulated base metal clusters because the high temperatures required for their reduction (> 1000 K) lead to their agglomeration and to the structural degradation of their crystalline microporous scaffolds [28,30]. In fact, these temperatures lead to the transformation of crystalline aluminosilicates into amorphous mesoporous solids [28] and to the formation of refractory metal aluminosilicates (e.g. $CoAl_2O_4$ [10]) or large metal particles at extracrystalline locations [30].

Several synthetic strategies have sought to circumvent the need for severe thermal treatments in order to avoid damage to the host frameworks. Concentrated sodium borohydride solutions (10 M) cause partial reduction ($< 50\%$) of Co^{2+}-exchanged FAU to form small (1.1 nm) encapsulated Co clusters [30]. Encapsulated Co nanoparticles have also been prepared in LTA and FAU zeolites by reducing exchanged Co^{2+} cations with treatment in Cd metal vapor [31]. Small Ni nanoparticles (< 5 nm diameter) were encapsulated within FAU by subliming $Ni(C_5H_5)_2$ complexes into zeolite micropores and subsequently decomposing the organic ligands via sequential photolysis with ultraviolet radiation and H_2 treatments [32]. Large (> 10 nm) Co_3O_4 particles have been embedded within defective regions in MFI crystals by using Co_3O_4/SiO_2 (instead of SiO_2) as the silica reagent in hydrothermal crystallization [33]. The impregnation of aqueous Fe $(NO_3)_3$•$9H_2O$ solutions onto NaOH-treated MFI (to form mesopores that enhance liquid imbibition) followed by thermal treatments in N_2 formed Fe_2O_3 particles about 20 nm in diameter, but present within mesopores, instead of being contained within the protecting MFI voids [34].

The mixed success and the system-specific nature of these techniques provide the impetus and rationale for the identification of the specific hurdles to achieving the encapsulation of base metal precursors while preventing the formation of refractory exchanged species or bulk compounds, and for the development of the robust general synthetic strategies reported here to circumvent these persistent hurdles. The challenges inherent in the encapsulation of base metals include the selection of stable precursors that can be embedded within zeolites, the difficult reduction of base metal cations when present as exchanged species, the enforcement of the selective placement of the precursors within intracrystalline regions, and the prevention of structural damage to zeolite frameworks during synthesis and subsequent thermal treatments.

This study addresses these hurdles through the hydrothermal assembly of zeolite frameworks around ligated metal precursors that promote metal uptake into zeolite crystals, protect metal precursors from precipitation or agglomeration during synthesis, preclude metal cation attachment to zeolite exchange sites, and preserve the structural integrity of the zeolites during crystallization and thermal treatments. In doing so, general procedures are described here for the successful encapsulation of Ni, Co, and Fe oxide clusters within LTA, MFI, and FAU. These procedures provide guiding principles and specific protocols that can be applied to metal-zeolite systems in general and well beyond the system-specific encapsulation of Co_3O_4 clusters within LTA that we reported previously [10].

Encapsulation is achieved here by adding Ni^{2+}, Co^{2+}, or Fe^{2+} cations protected by chelating ligands (N-[3-(trimethoxysilyl)propyl] ethylenediamine; TPE) into LTA, MFI, or FAU synthesis gels and allowing framework assembly to occur around them. The amine function in these bifunctional ligands chelates and protects metal cations from precipitation in the alkaline synthesis gels. The trimethoxysilyl moiety, in turn, forms siloxane linkages with nucleating zeolite precursors in order to enforce the incorporation of these precursors into the crystallizing frameworks. Oxidative treatments of the crystalline frameworks remove ligand species and form metal oxide particles, visible by transmission electron microscopy, that are small (< 2.5 nm) and uniformly distributed in size. The zeolite frameworks retain their crystallinity after oxidative treatment, in spite of local framework disruptions around the particles, because of the relatively low temperatures (623 K) required to detach metal cations from their chelating ligands and to nucleate oxide nanoparticles. The infrared spectra of adsorbed CO showed the absence of exchanged cations or bulk aluminosilicates, consistent with protecting ligands that preclude cation attachment at exchange sites. The stoichiometry and rates of reduction in H_2 of oxide nanoparticles confirmed their compositions (NiO, Co_3O_4, Fe_2O_3) and their facile reduction compared with metal aluminosilicates and exchanged cations. The presence of these species within the protected environment of LTA, MFI, and FAU frameworks was confirmed from catalytic rate measurements on samples with and without exposure to large organosulfur titrants that cannot enter intracrystalline regions.

These synthetic approaches circumvent each of the hurdles inherent in encapsulating base metal oxide particles and their precursors, thus enabling the preparation of diverse metal-zeolite compositions using the same general synthetic strategies. Such procedures, and the bifunctional ligands critical to their success, are thus broadly applicable beyond the specific systems used here to identify and circumvent these hurdles.

2. Experimental

2.1. Source and purity of reagents

$Ni(NO_3)_2$•$6H_2O$ (99.99%, Sigma-Aldrich), $CoCl_2$ (99.99%, Sigma-Aldrich), $FeCl_2$ (99.99%, Sigma-Aldrich), NiO (99.9%, Sigma-Aldrich), Co_3O_4 (99.9%, Sigma-Aldrich), Fe_2O_3 (99.9%, Sigma-Aldrich), N-[3-(trimethoxysilyl)propyl]ethylenediamine (TPE; 98%, Sigma-Aldrich), 1,4,7,10,13-pentaoxacyclopentadecane (15-C-5; 98%, Sigma-Aldrich), 1,4,7,10-tetraoxa-13-azacyclopentadecane (1-Aza-15-C-5; 97%, Sigma-Aldrich), Ludox AS-30 colloidal silica (30% wt. suspension in H_2O, Sigma-Aldrich), $NaAlO_2$ (53% Al_2O_3, 42.5% Na_2O, Riedel-de Haën), NaOH (99.99%, Sigma-Aldrich), tetraethyl orthosilicate (TEOS; 98%, Sigma-Aldrich), tetrapropylammonium hydroxide (TPAOH; 40% wt. in H_2O, Sigma-Aldrich), $CaCl_2$•$2H_2O$ (EMD Millipore), NH_4NO_3 (99.99%, Sigma-Aldrich), ethanol (99.9%, Sigma-Aldrich), 2,4,6-trimethylbenzyl mercaptan (TMBM; 98%, Sigma-Aldrich), fumed SiO_2 (Cab-O-Sil M5), acetone (99.9%, Sigma-Aldrich), air (extra dry; 99.999%, Praxair), He (99.999%, Praxair), 20% O_2/He (99.999%, Praxair), N_2 (99.999%, Praxair), 1% CO/He (99.999%, Praxair), Ar (99.999%, Praxair), and 4% H_2/Ar (99.999%, Praxair) were used as received. Deionized H_2O (17.9 Ω cm resistivity) was used in all procedures.

2.2. Materials synthesis

2.2.1. Synthesis of Ni, Co, and Fe oxide particles within LTA zeolites

NiO_x, CoO_x, and FeO_x were encapsulated within LTA zeolites (Si/

Al = 1) by adding Ni^{2+}, Co^{2+}, or Fe^{2+} cations protected against precipitation by chelating ligands into LTA synthesis gels, subsequently crystallizing these gels under hydrothermal conditions, and treating the crystalline powders in oxidative environments in order to remove the attached ligands and form metal oxide particles. Similar procedures were previously used to encapsulate Co_3O_4 clusters within LTA [10]; the synthetic procedures used here for the encapsulation of NiO_x and FeO_x in LTA were adapted and developed from this previous work in order to address significant synthetic hurdles arising from the tendency of metal cations to precipitate in alkaline solutions and difficulties in selectively converting encapsulated metal precursors into clusters. Such adaptations are intended to allow the encapsulation of metal oxide clusters within LTA through a generalized technique rather than system-specific methods, as were previously applied for the encapsulation of Co_3O_4.

The LTA-encapsulated materials were synthesized by first preparing solutions of the protecting ligand (N-[3-(trimethoxysilyl)propyl]ethylenediamine; TPE; 0.70–1.8 g) dissolved in deionized H_2O (9 cm^3). Separate aqueous solutions of $Ni(NO_3)_2\bullet6H_2O$, $CoCl_2$, or $FeCl_2$ (0.199–1.11 g in 9 cm^3 H_2O) were then added dropwise (~0.2 $cm^3\ s^{-1}$) to the aqueous ligand solutions while stirring with a magnetic bar (6.7 Hz). The amounts of ligand and metal precursor used for each sample were chosen to give a ligand(TPE)/metal(Ni, Co, Fe) molar ratio of 2, because at least two ligands per metal cation are required to protect the metal cations against precipitation in LTA synthesis gels (as shown in Section 3.1). These solutions were placed within polypropylene bottles (125 cm^3), and colloidal silica (5.3 g; Ludox AS-30) and NaOH (2.4 g) were sequentially added. The containers were sealed and heated to 353 K for 0.5 h while stirring at 6.7 Hz, and then cooled to ambient temperature. Solutions of $NaAlO_2$ (3 g) dissolved in H_2O (9 cm^3) were added, and the mixtures were held for 2 h at ambient temperature while stirring (6.7 Hz). These procedures lead to homogeneous LTA precursor synthesis gels (molar ratios 1.7 SiO_2/1.0 Al_2O_3/3.2 Na_2O/110 H_2O/0.098–0.27 metal/0.20–0.52 ligand), which were heated in the sealed bottles to 373 K and held for 12 h while stirring (6.7 Hz) in order to crystallize the intended LTA frameworks (NiLTA, CoLTA, FeLTA). The amount of Ni, Co, or Fe in the gels was chosen to achieve 2–5% wt. metal in the product solids, based on zeolite yields obtained in metal-free LTA syntheses. Synthesis gels were prepared with a range of metal loadings in order to identify the effect of metal content on product LTA crystallinity (determined by X-ray diffraction (XRD), Section 2.3.1); metal contents were systematically increased until only amorphous solids were detected in synthesis products (as discussed in Section 3.2.1).

The NiLTA, CoLTA, and FeLTA suspensions were filtered and rinsed with deionized H_2O until a pH of 7–8 was reached in the filtrate. The samples were treated in a convection oven at 373 K for 8 h and then heated in flowing dry air (1.67 $cm^3\ g^{-1}\ s^{-1}$) to 623 K (at 0.033 $K\ s^{-1}$) and held for 3 h. Treated samples were examined by X-ray diffraction (Section 2.3.1), electron microscopy (Section 2.3.2), and temperature programmed reduction (Section 2.3.4), and used in reactivity (Section 2.3.5) studies.

The LTA synthesis procedures form zeolites with Si/Al ratios of unity and Na^+ species as the charge-balancing cations [10]. Na^+ was exchanged by Ca^{2+} before NiLTA, CoLTA, and FeLTA samples were examined by infrared (IR) spectroscopy (Section 2.3.3) in order to assess their ability to bind CO at sub-ambient temperatures as a probe of the structure of metal species in the zeolites. The exchange of LTA with Ca^{2+} and other divalent cations (e.g., Co^{2+}) increases rates of intracrystalline CO diffusion, particularly at the sub-ambient temperatures used in the IR experiments in order to obtain detectable CO coverages [8,10]. Ca^{2+} exchange was carried out by adding NiLTA, CoLTA, or FeLTA solids (1 g) to 3 M aqueous $CaCl_2$ solutions (100 cm^3/g zeolite) and stirring for 8 h (at 6.7 Hz) at ambient temperature. Samples were then filtered and rinsed with deionized water (1500 $cm^3\ g^{-1}$), and the procedure was repeated thrice. These procedures lead to the essentially full exchange of Na^+ by Ca^{2+}, as confirmed by inductively-coupled plasma atomic emission spectroscopy (ICP-AES) measurements of the Ca and Al contents and Ca/Al ratio (Ca/Al = 0.5 [10]) in Ca^{2+}-exchanged LTA zeolites. The supernatant liquids remaining after Ca^{2+} exchange did not contain detectable Ni, Co, or Fe (ICP-AES), consistent with the absence of metal leaching during Ca exchange. Exchanged samples were treated in flowing dry air (1.67 $cm^3\ g^{-1}\ s^{-1}$) at 623 K (at 0.033 $K\ s^{-1}$) for 3 h before IR experiments (Section 2.3.3).

2.2.2. Synthesis of nickel oxide, cobalt oxide, and iron oxide clusters within MFI zeolites

Hydrothermal synthesis protocols for the preparation of MFI zeolites (Si/Al = 30 [35]) using tetrapropylammonium hydroxide (TPAOH) as an organic structure directing agent (SDA) were modified by incorporating the ligated metal cations described above into synthesis gels to prepare MFI frameworks containing NiO_x, CoO_x, and FeO_x clusters. The crystallization of the gels was followed by oxidative treatments of the product solids to remove the ligands and the SDA species.

NiMFI, CoMFI, and FeMFI samples were prepared using aqueous solutions of TPE (0.56–1.16 g ligand; 5 cm^3 H_2O) and aqueous solutions of $Ni(NO_3)_2\bullet6H_2O$, $CoCl_2$, or $FeCl_2$ (0.17–0.72 g in 5 cm^3 H_2O), which were added dropwise (~0.2 $cm^3\ s^{-1}$) to the aqueous ligand solutions while stirring (6.7 Hz) at ambient temperature. As in metal-LTA synthesis procedures (Section 2.2.1), TPE/cation (Ni^{2+}, Co^{2+}, or Fe^{2+}) molar ratios of 2 were used for all cations. TPAOH (40% wt. in H_2O; 8.27 g) and TEOS (17.3 g) were added sequentially to the ligand/cation solutions and stirred (6.7 Hz) for 13 h in sealed polypropylene bottles (125 cm^3) at ambient temperature. Separate solutions consisting of TPAOH (1 M in H_2O; 13.18 g), H_2O (0.40 g), and $NaAlO_2$ (0.189 g) were then added to the aged solutions containing TEOS, TPAOH, TPE, and metal cations. These mixtures were sealed within polypropylene bottles and heated at 371 K for 2 h while stirring (6.7 Hz). These procedures led to homogeneous synthesis gels (6.5 TEOS/2.3 TPAOH/0.18 $NaAlO_2$/120 H_2O/0.097–0.20 metal/0.19–0.4 ligand molar ratios), which were transferred into Teflon-lined stainless steel autoclaves (125 cm^3, Parr) and heated at 393 K for 15 h (for NiMFI and CoMFI) or 98 h (for FeMFI); the latter reflects MFI synthesis gels with ligated Fe precursors that require longer synthesis times to form crystalline products (as shown in Section 3.2.1). MFI synthesis gels were prepared with different metal contents in order to examine the effects of metal loading on product crystallinity (as discussed in Section 3.2.1). Metal contents were increased until amorphous products formed (determined by XRD; Section 2.3.1). These experiments led to MFI synthesis gels with metal contents chosen to obtain 2–4% wt. metal loading in MFI solids based on zeolite yields from metal-free MFI syntheses.

NiMFI, CoMFI, and FeMFI suspensions were filtered and rinsed with deionized water until the filtrate pH was 7–8 and then treated at 373 K in ambient air for 8 h. The samples were then heated in flowing dry air (1.67 $cm^3\ g^{-1}\ s^{-1}$) to 673 K (at 0.01 $K\ s^{-1}$) and held for 2 h before their use in X-ray diffraction (Section 2.3.1), electron microscopy (Section 2.3.2), infrared spectroscopy (Section 2.3.3), temperature programmed reduction (Section 2.3.4), and reactivity (Section 2.3.5) studies.

2.2.3. Synthesis of nickel oxide, cobalt oxide, and iron oxide clusters within FAU zeolites

Synthetic techniques for the hydrothermal crystallization of FAU [36] (Si/Al of 2.3) in the absence of an organic SDA were adapted and modified with the addition of base metal cations and protecting ligands to form encapsulated NiO_x, CoO_x, and FeO_x clusters. Hydrothermal assembly of FAU in the presence of ligated metal cations was followed by oxidative treatments to remove ligand species and form oxide clusters.

Synthesis gels were prepared by first dissolving TPE (0.61–1.92 g) and metal precursors ($Ni(NO_3)_2\bullet6H_2O$, $CoCl_2$, or $FeCl_2$; 0.18–1.16 g) in deionized H_2O (26.25 cm^3). TPE/cation molar ratios of 2 were used for all cations because two TPE ligands per metal cation are needed to prevent precipitation of the metal in FAU synthesis gels (as shown in Section 3.1). $NaAlO_2$ (2.34 g) and NaOH (3.77 g) were added sequentially while stirring (6.7 Hz; 0.25 h). Colloidal silica (28.6 g; Ludox AS-30) was then added to this solution at ambient temperature and stirred (at 6.7 Hz) for 2 h to prepare homogeneous synthesis gels (10 SiO_2/1.0 Al_2O_3/4.3 Na_2O/180 H_2O/0.093–0.29 metal/0.19–0.59 ligand molar ratios). The gels were sealed within 125 cm^3 polypropylene bottles and heated at 373 K for 12 h without stirring to form NiFAU, CoFAU, or FeFAU solids. FAU synthesis gels were prepared with a variety of metal contents in order to identify effects of metal loading on product zeolite crystallinity (as discussed in Section 3.2.1). Gels with progressively higher metal contents were prepared until amorphous products were formed by the above procedures, as determined by XRD (Section 2.3.1). The metal content in these gels was chosen to achieve 1–3% wt. metal in products (based on zeolite yields in metal-free syntheses). NiFAU, CoFAU, or FeFAU products were isolated by filtration and rinsed to a filtrate pH of 7–8. These solids were then treated in a convection oven at 373 K for 8 h in ambient air and heated in flowing dry air (1.67 $cm^3\,g^{-1}\,s^{-1}$) to 623 K (at 0.033 $K\,s^{-1}$) and held for 3 h. The treated samples were then used in characterization (Section 2.3.1-2.3.4) and reactivity (Section 2.3.5) studies.

Chelating compounds including crown ethers (1,4,7,10,13-pentaoxacyclopentadecane; 15-C-5) and heterocyclic amines (e.g., 1,4,7,10-tetraoxa-13-azacyclopentadecane; 1-Aza-15-C-5) were examined for their potential dual use as both stabilizing ligands for metal cations and templating agents for FAU assembly. Such species were intended to combine the functionality of the chelating ligand and zeolite templating agent in order to avoid competition for intracrystalline void space by distinct ligand and templating species (Section 3.2.1). The ability of these heterocyclic compounds to stabilize metal cations (Ni^{2+}, Co^{2+}, Fe^{2+}) was examined by preparing aqueous solutions with ligand/metal ratios of 1 at concentrations equivalent to those used in the FAU synthesis gels described above. These solutions were then brought to pH 13 using NaOH and heated to the crystallization temperature (373 K) as they were monitored for the formation of solid precipitates.

2.2.4. Ion exchange of LTA, MFI, and FAU zeolites with Ni^{2+}, Co^{2+}, or Fe^{2+} cations

LTA, MFI, and FAU zeolites prepared in the absence of ligands or metal cations were post-synthetically exchanged with Ni^{2+}, Co^{2+}, or Fe^{2+} cations in order to provide a comparison with samples prepared by direct hydrothermal synthesis in the presence of ligated cations (Section 2.2.1-2.2.3). These samples were used in infrared (IR) spectroscopy experiments (Section 3.3.1) in order to obtain the spectra for CO bound at exchanged cations and to demonstrate the absence of such species in samples prepared by direct hydrothermal syntheses. The LTA, MFI, and FAU zeolites used for ion exchange with Ni^{2+}, Co^{2+}, or Fe^{2+} were synthesized via hydrothermal synthesis as described in Sections 2.2.1-2.2.3, but in the absence of TPE ligands or metal precursors.

The exchange of Ni, Co, and Fe cations to replace charge-balancing Na^+ species was carried out on LTA (Si/Al = 1) and FAU (Si/Al = 2.3) by dispersing zeolite powders (3 g) in deionized water (10 cm^3) and adding $Ni(NO_3)_2{\bullet}6H_2O$, $CoCl_2$, or $FeCl_2$ precursors at concentrations required to give 3% wt. metal contents at full uptake, which correspond to metal(Ni, Co, Fe)/Al ratios of 0.09 and 0.12 for LTA and FAU, respectively. A nominal metal content of 3% wt. was chosen for these samples because it resembles the metal loadings in samples formed by direct hydrothermal syntheses with ligated precursors (2–4% wt.; Section 3.2). Aqueous mixtures of zeolites and metal cations were placed within polypropylene bottles and stirred (6.7 Hz) at ambient temperature for 12 h. In the case of Fe^{2+}, exchange was performed in a N_2 atmosphere to inhibit the formation of Fe^{3+}. The exchanged zeolites were isolated by filtration, rinsed with deionized H_2O (1500 $cm^3\,g^{-1}$), and treated in ambient air at 373 K for 8 h. Their metal contents (2.5–3.0% wt., ICP-AES) were consistent with nearly full uptake of metal cations.

Exchange protocols for MFI (Si/Al = 30) zeolites were adapted from previous reports [37]; they differ from those used for LTA (Si/Al = 1) and FAU (Si/Al = 2.3) because the exchange of divalent cations into high-silica zeolites is hindered by the low prevalence of adjacent Al pairs required to dehydrate cation solvation shells and allow their attachment to the framework [38]. The low Al content in MFI (Si/Al = 30; formula $Na_{3.1}[Al_{3.1}Si_{92.9}O_{192}](H_2O)_{16}$ [35]) limits the maximum metal content that can be achieved at full exchange (2.8–2.9% wt. for (Ni,Co,Fe)/Al = 1, assuming the absence of extra-framework alumina) and precludes full exchange when Al next nearest neighbors are required to anchor divalent cations [37]. Cation exchange was encouraged by the use of above-ambient temperatures and longer exchange times than for LTA and FAU. The H-form instead of the Na-form of MFI was also used to prevent the localized precipitation of $Co(OH)_2$ in zeolite channels during exchange, which can occur when the exchange is conducted at elevated temperature (353 K) over an extended period of time [39].

Metal-free MFI samples were first exchanged with NH_4^+ cations by suspending MFI powders (2.5 g) in aqueous 0.5 M NH_4NO_3 (50 cm^3) and stirring (6.7 Hz) at 353 K for 10 h. The solids were recovered by filtration and rinsed with deionized H_2O (1500 $cm^3\,g^{-1}$); this procedure was repeated two more times. H-MFI was then treated in ambient air at 373 K for 12 h, and then in flowing dry air (1.67 $cm^3\,g^{-1}\,s^{-1}$) at 773 K for 20 h. This process leads to the nearly complete exchange of Na^+ for H^+ (< 0.1% wt. residual Na) [37]. H-MFI solids were then suspended in 0.05 M $Ni(NO_3)_2{\bullet}6H_2O$, $CoCl_2$, or $FeCl_2$ solutions (250 $cm^3\,g^{-1}$) and stirred (6.7 Hz) at 353 K for 16 h in ambient air (Co^{2+}, Ni^{2+}) or a N_2 atmosphere (Fe^{2+}). The solids were recovered by filtration, rinsed with deionized water (1500 $cm^3\,g^{-1}$), and treated in ambient air at 373 K for 8 h. ICP-AES analysis indicated partial exchange was achieved (cation/Al = 0.04, 0.03, and 0.02 corresponding to 0.12% wt., 0.09% wt., and 0.06% wt. for Ni^{2+}, Co^{2+}, and Fe^{2+}). These low metal contents reflect the small fraction of Al sites present as Al-Al next nearest neighbors in Si-rich zeolites [38]. These metal contents, however, are sufficient to allow exchanged metal species to be probed by infrared spectroscopy (Section 3.3.1) and temperature-programed reduction (Section 3.3.2).

2.3. Characterization of zeolite structures and of the size, stoichiometry, and encapsulation selectivity of metal oxide clusters

2.3.1. X-ray diffraction

X-Ray diffraction (XRD) was used to determine the structure and crystallinity of the metal-zeolite samples and to detect the presence of any large metal oxide crystallites (> 10 nm). Diffractograms were measured using a D8 Discover GADDS Powder Diffractometer with Cu-Kα radiation ($\lambda = 0.15418$ nm, 40 kV, 40 mA) over a 2θ range of 5–50° (0.00625° s^{-1}) on ground powders dispersed uniformly onto quartz slides. The crystallinities of metal-zeolite samples were determined quantitatively from the integrated intensities of the three most intense Bragg lines present in the diffractograms, using metal-free LTA, MFI, and FAU as standards (Section 2.2).

2.3.2. Transmission electron microscopy

Size distributions of metal oxide nanoparticles were measured by transmission electron microscopy (TEM). A Philips/FEI Tecnai 12 microscope operating at 120 kV was used to obtain micrographs on samples prepared by dispersing ground powders in acetone and then onto holey carbon films mounted on 400 mesh copper grids (Ted Pella Inc.). Particle size distributions were based on measurements of > 300 particles for each sample; these distributions were used to calculate surface-averaged particle diameters $< d_{\mathrm{TEM}} >$ [40]:

$$\langle d_{\mathrm{TEM}} \rangle = \frac{\sum n_i d_i^3}{\sum n_i d_i^2} \tag{1}$$

where n_i is the number of clusters with diameter d_i. The dispersion of these particles (D), defined as the fraction of metal (Ni, Co, Fe) atoms present at the surface of the metal oxide clusters, was determined using [40]:

$$D = 6\frac{\nu_m/a_m}{\langle d_{\mathrm{TEM}} \rangle} \tag{2}$$

where ν_m is the atomic volume of Ni atoms in bulk NiO (0.0183 nm^3 [41]), Co atoms in bulk Co_3O_4 (0.0222 nm^3 [42]), or Fe atoms in bulk Fe_2O_3 (0.0256 nm^3 [43]); and a_m is the area per fully exposed atom on the (001) plane of NiO (0.0877 nm^2 [41]), the (100) plane of Co_3O_4 (0.164 nm^2 [42]), and on the (0001) plane of Fe_2O_3 (0.0841 nm^2 [43]).

Particle size distributions were also used to determine dispersity indices (DI) for each sample; these values are defined as the surface-averaged particle diameter ($< d_{\mathrm{TEM}} >$) divided by the arithmetic mean diameter ($< d_{\mathrm{n}} >$) [40]:

$$\mathrm{DI} = \frac{\langle d_{\mathrm{TEM}} \rangle}{\langle d_n \rangle} = \frac{\left(\frac{\sum n_i d_i^3}{\sum n_i d_i^2}\right)}{\left(\frac{\sum n_i d_i}{\sum n_i}\right)} \tag{3}$$

The DI constitutes a rigorous metric for particle size uniformity; sets of particles with DI values smaller than 1.5 are typically considered to be narrowly distributed in size [40].

2.3.3. Infrared spectra of adsorbed CO on samples prepared by direct hydrothermal synthesis and post-synthetic exchange

Metal-zeolite samples prepared by direct hydrothermal synthesis (Section 2.2.1-2.2.3) and post-synthesis exchange (Section 2.2.4) were exposed to CO, and their infrared (IR) spectra were collected in order to detect the presence of exchanged metal cations or metal aluminosilicate compounds. NiLTA, CoLTA, and FeLTA samples prepared via hydrothermal synthesis were used in their Ca^{2+}-exchanged form because substitution of monovalent Na^+ with divalent cations (e.g., Ca^{2+}, Co^{2+}) allows more facile access by CO into intracrystalline regions (Section 2.2.1). Spectra were measured using sample wafers (40 mg cm^{-2}) and a Thermo Nicolet 8700 spectrometer equipped with an in-situ flow cell. Samples were heated (at 0.033 K s^{-1}) in flowing N_2 (40 $\mathrm{cm}^3\,\mathrm{g}^{-1}\,\mathrm{s}^{-1}$) to 523 K and held for 1 h before exposure to CO. They were then cooled to 273 K and exposed to flowing 1% CO/He (40 $\mathrm{cm}^3\,\mathrm{g}^{-1}\,\mathrm{s}^{-1}$) for 0.25 h before measuring spectra. The spectral contributions from CO(g), CO bound at Ca^{2+} or Na^+ cations [44], and CO physisorbed onto the aluminosilicate framework were subtracted using the corresponding spectra for metal-free LTA, MFI, and FAU. Low CO pressures (1.0 kPa) were used in order to minimize CO adsorption onto Ca^{2+} and Na^+ charge-balancing cations [44] and on surfaces of oxide crystallites [45–47], which would interfere with the accurate detection of CO bands on metal aluminosilicates or exchanged Ni^{2+}, Co^{2+}, and Fe^{2+} cations.

2.3.4. Rate and stoichiometry of reduction for samples prepared by direct hydrothermal synthesis and post-synthetic ion exchange

The reduction stoichiometries and rates for each sample were measured using temperature-programmed reduction (TPR) methods and a Micromeritics AutoChem II 2920 analyzer system equipped with a thermal conductivity detector (TCD) in order to measure H_2 concentrations in the outlet stream. Samples (0.02–0.50 g) were placed within U-shaped quartz tubes and heated to 313 K in flowing Ar (0.83 $\mathrm{cm}^3\,\mathrm{s}^{-1}$) for 0.33 h, and then exposed to flowing 4% H_2/Ar (0.83 $\mathrm{cm}^3\,\mathrm{s}^{-1}$) and heated to 1273 K at 0.167 K s^{-1}. The TCD response was calibrated using the stoichiometric reduction of bulk Co_3O_4 and used to calculate H_2 consumption rates as a function of extent of reduction and temperature.

2.3.5. Encapsulation selectivities from ethanol oxidative dehydrogenation rates with and without titration of external particles

Ethanol (EtOH) oxidative dehydrogenation (ODH) rates before and after selective titration of extracrystalline oxide surfaces were measured on all metal-zeolite samples in order to determine the extent of encapsulation of metal oxide nanoparticles within zeolite voids. Metal-zeolite samples were exposed to a bulky organosulfur titrant (2,4,6-trimethylbenzyl mercaptan; TMBM) that cannot readily diffuse through the zeolite apertures. EtOH ODH rates on these samples, on untitrated samples, and on the respective bulk oxides (NiO, Co_3O_4, Fe_2O_3) were compared to determine the fraction of the oxide surface areas residing within the protected environment of the zeolite voids (Section 3.4).

Metal-zeolite and bulk oxide samples were exposed to TMBM before ethanol ODH reactions by suspending the powder samples (0.1 g) in 0.2 M solutions of TMBM in EtOH (15 cm^3). The suspensions were stirred (6.7 Hz) at ambient temperature for 2 h (Ni, Co) or 16 h (Fe). Longer exposure times were found to be required in order to titrate bulk Fe oxide surfaces (Section 3.4). Solids were isolated by filtration and treated in ambient air at 373 K for 8 h. These procedures were used, but without TMBM in the liquid EtOH solution, in order to prepare the untitrated control samples used as comparisons.

The titrated and control samples were diluted (10-fold by mass) with SiO_2 and pelleted and sieved to retain aggregates 180–250 μm in size in order to avoid any temperature gradients from exothermic oxidation reactions. These aggregates were placed within fritted quartz tubes (8 mm I.D.) and heated to 393 K in flowing 20% O_2/He (1.67 $\mathrm{cm}^3\,\mathrm{g}^{-1}\,\mathrm{s}^{-1}$). Temperature was controlled using a three-zone resistively-heated furnace equipped with Watlow Series 988 electronic controllers and measured with a type-K thermocouple (Omega, Inc.) attached to the outer tube surface. Liquid EtOH was introduced into an O_2/He stream using a syringe pump (Cole Parmer; 60061 Series) through a port held at 393 K. Gas flow rates were metered using Porter Instrument mass flow controllers set to achieve the desired EtOH, O_2, and He pressures (4 kPa EtOH, 9 kPa O_2, 87 kPa He). EtOH conversions were kept below 3% and all transfer lines were heated to 393 K to prevent condensation of reactants or products.

Turnover rates for EtOH ODH are reported here based on the number of surface atoms determined from metal contents and dispersions for metal-zeolite samples (Eq. (2)) and from BET surface areas and atom surface densities for bulk oxides (Supporting Information (SI), Section S1). Effluent concentrations of EtOH and acetaldehyde, the only product detected, were measured by flame ionization after chromatographic separation (phenylmethyl-silicone capillary column; HP-5; 50 m × 0.32 mm, 1.05 μm film thickness; Shimadzu GC-2014). Deactivation was not detected in the time scale of these experiments (~8 h). Empty reactors, mesoporous silica, and metal-free LTA, MFI, and FAU did not lead to detectable amounts of any EtOH oxidation products.

3. Results and discussion

3.1. Assessing the stability of ligated metal precursors in zeolite synthesis gels

The stability of coordination complexes formed from Ni^{2+}, Co^{2+}, and Fe^{2+} cations and ligands (N-[3-(trimethoxysilyl)propyl]ethylenediamine; TPE) was examined by treating these complexes at the pH and temperature required for the crystallization of each zeolite framework in order to detect colloidal precipitation. Scheme 1 shows the schematic structure of TPE; also shown in Scheme 1 are other heterocyclic chelating complexes used (or proposed for use) in this work as bifunctional stabilizing ligands and organic structure directing agents, specifically for the synthesis of metal-FAU samples (Section 3.2.1). TPE was chosen as the stabilizing ligand because of its bidentate amine functionality, which is known to chelate metal cations [48,49], and is thus able to confer resistance to precipitation of cations as hydroxides in alkaline solutions [10]. Temperatures (373–393 K), pH levels (13–14), and

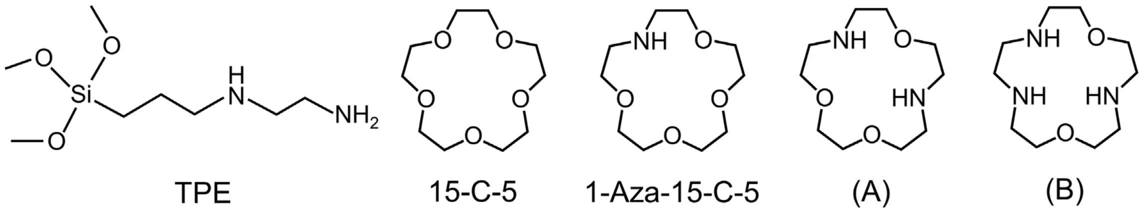

Scheme 1. Chelating agents and ligands mentioned and/or used in this work: N-[3-(trimethoxysilyl)propyl]ethylenediamine (TPE); 1,4,7,10,13-pentaoxacyclopentadecane (15-C-5); 1,4,7,10-tetraoxa-13-azacyclopentadecane (1-Aza-15-C-5); 1,4,10-trioxa-7,13-diaza-cyclopentadecane (A); 1,7-dioxa-4,10,13-triazacyclopentadecane (B).

concentrations of solvated cations (0.03–0.09 M) used for the stability tests were chosen to reflect those required to crystallize LTA, MFI, and FAU (Section 2.2). Solutions with TPE/cation ratios of unity formed solid precipitates, even at temperatures lower than required to form LTA and FAU (373 K; Section 2.2.1, 2.2.3) for all cations, consistent with the displacement of the ligands by OH^- and the formation of oxyhydroxides. Ni^{2+}, Co^{2+}, and Fe^{2+} solutions prepared with TPE/cation ratios of 2, in contrast, did not precipitate even after 100 h at the conditions required to form LTA, MFI, or FAU (373–393 K; Section 2.2.1-2.2.3). These data show that TPE ligands stabilize Ni^{2+}, Co^{2+}, and Fe^{2+} cations at molar ratios of 2 or higher. Monodentate amine ligands, such as NH_3, were unable to prevent precipitation of Co cations even at NH_3/Co ratios of 6 at LTA synthesis conditions [10]. The stability against precipitation of metal precursors conferred by TPE ligands requires the chelating action that is provided by the bidentate amine moiety. The use of these TPE ligands therefore overcomes one of the principal hurdles in the encapsulation of base metals by preventing the formation of oxyhydroxides at the temperature and pH conditions required for framework nucleation and growth. The ability of the TPE ligands to stabilize all three cationic species (Ni^{2+}, Co^{2+}, Fe^{2+}) at the conditions of hydrothermal synthesis demonstrates the versatility of these ligand species and their general applicability, in spite of the differing tendencies of these three cations to precipitate in alkaline solutions.

3.2. Synthesis of crystalline zeolite frameworks and their stability during thermal treatment protocols

3.2.1. Effects of the ligand and metal contents of synthesis gels on the crystallinity of zeolites prepared by hydrothermal synthesis

The presence of ligated cations in zeolite synthesis gels can inhibit or even prevent crystallization when such species are present at sufficiently high concentrations and occupy volumes larger that the framework voids [8,10]. The alkoxysilane moiety in TPE enforces the uptake of ligated precursors within the void structure by forming siloxane bridges with the framework as nuclei form and grow [8–10]. Such siloxane linkages and the bulky nature of these coordination complexes, however, can locally disrupt zeolite crystal periodicity [8,10]. The size of Ni^{2+}, Co^{2+}, and Fe^{2+} cations with two attached TPE ligands (~1.1 nm, ~1.0 nm, and 1.1 nm, respectively; estimated by MolView, v. 2.2, largest dimension [50]) is similar or slightly larger than the α-cage diameters in LTA (1.1 nm [51]) and FAU (1.1 nm [51]) or the channel intersections in MFI (0.64 nm [51]), indicating that the framework structures must distort locally when these complexes are occluded within intracrystalline voids. This imposes limits on the volumetric density of ligated precursors that can be placed within frameworks without preventing their nucleation and, consequently, on the loading of metal cations (and ultimately of metal and oxide particles) that can be encapsulated via direct hydrothermal syntheses.

Metal-zeolite samples with 2–5% wt. metal content in their synthesis gels were prepared in order to determine the highest metal loadings that could be attained without compromising framework crystallinity. The results, including the metal and ligand contents in synthesis gels and the crystallinity of the solids formed, are summarized in Table 1.

Table 1
Metal species, targeted framework, nominal metal loading, ligand content, and crystallinity of synthesized solids for the synthesis of metal-zeolite samples.

Metal	Zeolite Synthesis Gel	Nominal metal loading (% wt.)[a]	TPE/T-atom[b]	% Crystallinity[c]
Ni	LTA	4	0.089	98
	LTA	5	0.11	0
	MFI	3	0.042	97
	MFI	4	0.055	3
	FAU	2	0.030	99
	FAU	3	0.043	16
Co	LTA	4	0.088	96
	LTA	5	0.11	3
	MFI	3	0.042	96
	MFI	4	0.055	5
	FAU	2	0.030	99
	FAU	3	0.043	1
Fe	LTA	3	0.071	95
	LTA	4	0.093	0
	MFI	2	0.030	95
	MFI	3	0.044	7
	FAU	2	0.032	98
	FAU	3	0.046	2

[a] Metal loading that would result if all metal added to the synthesis gel were incorporated into the synthesized solids, assuming solid yields equivalent to metal and ligand-free LTA, MFI, or FAU syntheses.

[b] Molar ratio of TPE ligands to the total number of T atoms (T = Si, Al) in the synthesis gel.

[c] Determined by XRD. Diffractograms shown in supporting information, Sections S2 (LTA), S3 (MFI), and S4 (FAU). Calculated from integrated intensities of the three most intense Bragg lines using metal-free LTA, MFI, and FAU as standards (Section 2.3.1).

Our previous studies showed CoLTA samples could be prepared with up to 4% wt. Co, but higher loadings prevented LTA crystallization [10]. X-Ray diffractograms of NiLTA and FeLTA prepared with 4% wt. and 3% wt. metal loading, respectively, gave sharp Bragg lines indicative of crystalline LTA structures (Section S2, SI). NiLTA and FeLTA samples synthesized with 5% wt. and 4% wt. nominal metal contents, however, gave diffuse backgrounds without detectable diffraction lines, consistent with the prevalence of amorphous solids (XRD; Section S2, SI).

Similar effects of higher loadings were evident for MFI and FAU frameworks. NiMFI, CoMFI, and FeMFI with 3%, 3%, and 2% metal contents in the synthesis gels gave the diffraction patterns of crystalline MFI, while higher loadings (4%, 4%, and 3%) gave amorphous samples (Section S3, SI). Metal-FAU samples (NiFAU, CoFAU, and FeFAU) were crystalline for nominal metal contents as high as 2% wt., but were amorphous when prepared with 3% wt. nominal loadings (Section S4, SI). The ratios of TPE ligands to T atoms (T = Si, Al) present in LTA, MFI, and FAU synthesis gels leading to the highest metal contents that allowed framework crystallization were 0.07–0.09, 0.03–0.04, and 0.03, respectively. These ratios were similar for gels containing Ni or Co cations (LTA: 0.09, MFI: 0.04, FAU: 0.03) and slightly lower for LTA and MFI gels containing Fe cations (LTA: 0.07, MFI: 0.03, FAU: 0.03), showing that the addition of Fe, instead of Ni or Co, to the synthesis gels places more stringent limits on the maximum attainable loadings. The TPE/T-atom ratios present in synthesis gels at these maximum attainable loadings show that crystalline zeolites can form even when up to 9% of T-atoms are derived from the alkoxysilane moieties in the TPE ligands, demonstrating that zeolite self-assembly processes are quite tolerant of the disruptions imposed by the TPE ligands. These data establish upper limits to attainable metal loadings and confirm that ligated metal precursors can disrupt zeolite crystallization when present at sufficiently high concentrations.

The mechanistic basis of these specific limits for each given framework and metal remain speculative. These limits may reflect the fraction of the silicates/aluminates in gels that form linkages with the TPE siloxy groups (present at TPE/cation ratios of 2). These linkages serve to anchor metal precursors to aluminosilicate oligomers during zeolite crystal growth [8–10], but also appear to disrupt framework assembly by displacing the cations (Na^+, TPA^+) that template the crystallization of a given framework, while also possibly forming these framework attachments at positions ill-suited for ultimate nucleation and growth. Such disruptions may be caused by steric effects from the ligand alkyl chain, which interfere with crystal growth by preventing the attachment of aluminosilicate oligomers or by distorting their orderly attachment to pre-existing framework nuclei. The maximum ligand contents (and thus metal contents) that allow crystallization for LTA, MFI, and FAU synthesis gels (TPE/T-atom ratios: 0.09, 0.04, 0.03) differ among these frameworks; they do not systematically correlate with framework density (LTA: 14.2, MFI: 18.4, FAU: 13.3; units: T-atom $(1000\,Å^3)^{-1}$) [51], with the largest void size (LTA: 1.1 nm, MFI: 0.64 nm, FAU: 1.1 nm) [51], with the molar ratios of templating cations (Na^+ for LTA, FAU; TPA^+ for MFI) to metal cations (LTA: 30, MFI: 16, FAU: 44) in the synthesis gels, with Si/Al ratios (LTA: 1.0, MFI: 30, FAU: 2.3), or with the mean crystal diameter (from TEM; LTA: ~600 nm, MFI: ~200 nm, FAU: ~800 nm).

Ligated Fe precursors appear to impose more significant hurdles to crystallization than Ni or Co precursors, as evident from the lower metal contents attainable for Fe-containing samples (Table 1). FeMFI synthesis gels (1.5% wt. nominal loading) held at hydrothermal synthesis conditions for 15 h formed viscous liquids without detectable solids, while NiMFI and CoMFI synthesis gels with 1.5% wt. metal formed crystalline solids after 15 h (Fig. 1). Longer crystallization times (98 h; Section 2.2.2) ultimately led to the formation of MFI crystals in FeMFI gels (Fig. 1). These more significant hurdles imposed by ligated Fe precursors at similar molar contents in gels may reflect the different binding orientations of TPE ligands to Fe cations, which could impose greater local disruptions to the assembly of aluminosilicate oligomers.

At a specific pH and temperature, Fe^{3+} cations can be inserted into zeotype frameworks [52,53] through the formation of Si-O-Fe linkages [53]. The formation of such linkages in Fe-zeolite synthesis gels would require the oxidation of ligated Fe^{2+} cations to Fe^{3+} and the displacement of the attached TPE ligands. Ligand detachment would allow the formation of the Si-O-Fe linkages required to adopt the tetrahedral coordination of framework T-sites, which would have been evident from the rapid precipitation of ligated precursors during stability tests (Section 3.1), because ligand detachment in the absence of Si or Al sources would have led to the formation of Fe-O-Fe linkages and to the nucleation of colloidal oxyhydroxides. Indeed, ligated Ni, Co, and Fe precursors form oxide clusters instead of framework heteroatoms after oxidative treatments, as shown by the infrared (Section 3.3.1), reduction (Section 3.3.2), and reactivity (Section 3.4) data below.

The 1,4,7,10,13-pentaoxacyclopentadecane (15-C-5 crown ether; Scheme 1) ligand was examined as an alternative to TPE ligands for cation stabilization during the synthesis of FAU, which had the lowest attainable metal content of the three zeolite frameworks prepared from TPE-stabilized cations (2% wt.; Table 1). 15-C-5 forms chelate complexes with divalent first-row transition metal cations such as Ni^{2+}, Co^{2+}, and Fe^{2+} [54], and also acts as an organic structure-directing agent (OSDA) [55]. 15-C-5 is incorporated into FAU crystals during the framework assembly process [55]; however, unlike TPE, 15-C-5 does not form siloxane linkages with zeolite precursors and therefore does not disrupt crystal periodicity. As a result, the use of 15-C-5 as a chelating agent for metal cations could provide a route to forming crystalline zeolites with higher metal loading than can be achieved with TPE ligands. Solutions with (15-C-5)/cation ratios of unity, however, led to fast precipitation of metal precursors at a pH of 13, indicative of the displacement of the chelating crown ethers by OH^-. We conclude that the interactions between cations and the O-atoms in 15-C-5 are much weaker than the coordinative attachments formed between cations and the two amine groups in TPE [54]. The use of 1,4,7,10-tetraoxa-13-azacyclopentadecane crown ethers (1-Aza-15-C-5; Scheme 1), which contain a secondary amine instead of one of the O-atoms as part of the heterocycle, also led to fast precipitation at ambient temperature and a pH of 13. Identical experiments conducted with ligand/cation ratios of 2 also led to precipitation using either 15-C-5 or 1-Aza-15-C-5 ligands.

Metal cation interactions with amine groups are generally stronger than with O-atoms within crown ethers [54], but interactions with a single amine group are insufficient to prevent ligand displacement by OH^- at the pH required for hydrothermal syntheses. We surmise that 15-C-5 cyclic species with more than one amine moiety, such as 1,4,10-trioxa-7,13-diaza-cyclopentadecane and 1,7-dioxa-4,10,13-triaza-cyclopentadecane (Scheme 1), may provide the requisite stability at the

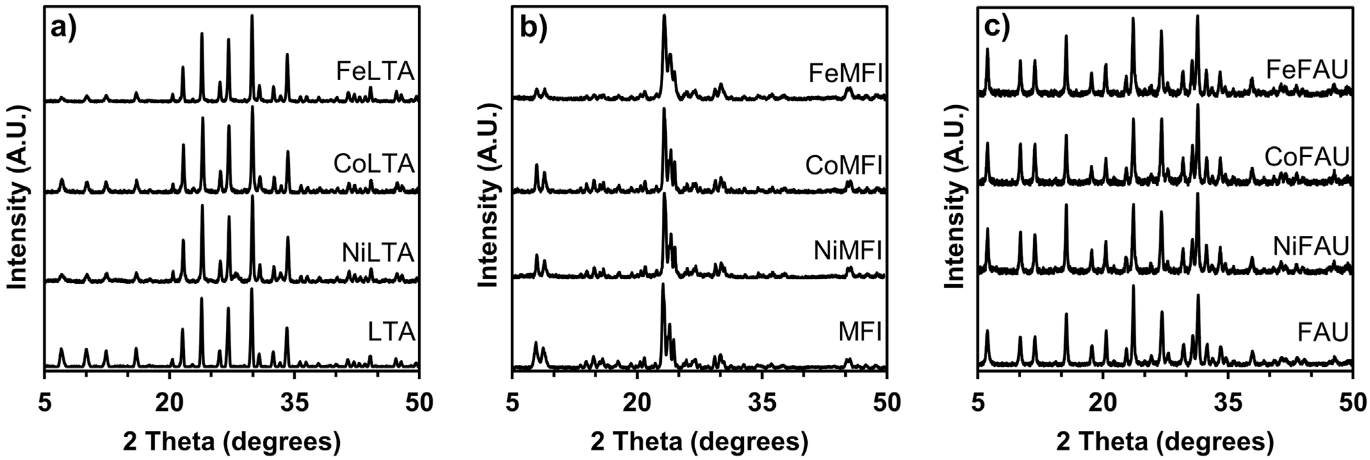

Fig. 1. X-Ray diffractograms of a) metal-LTA, b) metal-MFI, and c) metal-FAU samples prepared via hydrothermal assembly in the presence of ligated metal precursors and comparative metal-free samples prepared using the procedures in Section 2.2. Diffractograms were collected on samples following their post-synthetic oxidative treatment in flowing dry air ($1.67\,cm^3\,g^{-1}\,s^{-1}$; $0.033\,K\,s^{-1}$; 623 K; 2 h).

Table 2
Metal loadings, particle diameters, particle dispersions, and particle dispersity indices of metal-zeolite samples.

Sample	Metal loading (% wt.)[a]	Particle diameter $< d_{TEM} >$ (nm)[b]	Fractional dispersion (D)[c]	Dispersity index (DI)[d]
NiLTA	2.7 (3.0)	1.5 ± 0.2	0.81	1.04
NiMFI	1.3 (1.5)	1.9 ± 0.3	0.66	1.06
NiFAU	1.4 (1.5)	2.3 ± 0.4	0.55	1.10
CoLTA	2.6 (3.0)	1.6 ± 0.3	0.51	1.06
CoMFI	1.3 (1.5)	1.7 ± 0.2	0.47	1.03
CoFAU	1.4 (1.5)	2.2 ± 0.4	0.37	1.09
FeLTA	2.5 (3.0)	1.9 ± 0.3	0.74	1.07
FeMFI	1.2 (1.5)	1.9 ± 0.3	0.74	1.05
FeFAU	1.2 (1.5)	2.2 ± 0.4	0.62	1.09

[a] Measured for crystallized samples after oxidative treatment using inductively coupled plasma optical emission spectroscopy. Nominal metal loading in synthesis gels shown in parentheses.

[b] Surface-averaged cluster diameter determined by TEM (Eq. (1)).

[c] Particle dispersion estimated using $< d_{TEM} >$ (Eq. (2)).

[d] Particle dispersity index calculated as the surface-averaged cluster diameter divided by the arithmetic mean diameter (Eq. (3)).

conditions of hydrothermal syntheses. The use of such heterocyclic amines as chelating agents for metal cations could also serve to provide organic templates for FAU synthesis, as in the case of 15-C-5. The dual nature of these heterocyclic amines, as templates and protecting ligands, would also avoid the exclusion of the template, required for framework crystallization, from intracrystalline voids by the competing presence of a separate ligated cation complex. Such ligand-template species would open new routes to confine metal and oxide nanoparticles within FAU or other zeolites that use crown ethers as templates at metal loadings even higher than those attainable by the synthesis protocols reported here. The search for molecules that act as templates for other structures, but which also stabilize metal cations, would make these synthetic strategies applicable in general for broader classes of zeolites and nanoparticle compositions and with fewer inherent limits on attainable metal contents.

These results, taken together, demonstrate the ubiquitous hurdles that interfere with the concurrent need to stabilize metal precursors with ligands that also encourage their inclusion within the void structure, but which do not disrupt the nucleation and growth of the microporous frameworks. They also provide the guidance and protocols required to circumvent them, to the extent allowed by the nature of the ligands that prevent the precipitation of precursors at the pH and temperature needed for hydrothermal crystallization. Ligated precursors in synthesis gels, when present in excess of a critical concentration, disrupt the formation of periodic framework structures and limit the attainable metal contents. Consequently, these critical concentrations in the synthesis must be determined, by experimentation at the current time, in order to ensure successful encapsulation. Specific metal precursors, such as Fe^{2+} cations, can impose nucleation barriers that can be addressed by longer synthesis times. Structure-directing molecules with functional groups that prevent precursor precipitation would avoid the inherent compromises between metal content and framework crystallinity. Such species would serve the dual function to template framework assembly and to chelate metal precursors, thus eliminating disruptions to framework assembly caused by covalent linkages between ligands and framework precursors and by the displacement of templating agents by ligands from within zeolite voids. In the next section, we describe protocols and practices intended to preserve zeolite crystallinity during the post-synthetic treatments required to convert ligand-protected metal precursors occluded within zeolites into nanoparticles.

3.2.2. Zeolite crystallinity and oxide formation after ligand removal via thermal treatments

Post-synthetic treatments are required to remove ligands and transform ligated precursors into metal or oxide particles; such treatments can disrupt framework structures when high temperatures are required. The reduction of zeolite-exchanged base metal cations to metal nanoparticles, for instance, requires treatments in H_2 above 1000 K [28], which destroy aluminosilicate frameworks and form large metal crystallites within the amorphous aluminosilicates that form [28,30]. The chelating TPE ligands used here were chosen with the intent of preventing, through preferential coordination and steric hindrance, direct linkages between metal cations and framework T-sites, thus allowing the conversion of these precursors into oxide clusters at temperatures lower than those required to reduce exchanged cations. Temperature-programmed oxidation studies on CoLTA showed that TPE ligands can be removed by oxidative treatments at 623 K, without affecting the host framework or leading to the grafting of Co^{2+} cations onto LTA exchange sites [10].

The metal-zeolite samples prepared here by direct hydrothermal synthesis using TPE-ligated metal precursors were treated in oxidative environments (21% O_2) at 623–673 K (Section 2.2.1-2.2.3) in an attempt to remove the organic ligands (TPE) and the MFI OSDA (TPAOH; Section 2.2.2). The structural integrity of zeolite frameworks and the presence of nanoparticles in the treated samples were determined by XRD (Section 2.3.1) and TEM (Section 2.3.2), respectively.

The X-ray diffractograms for samples prepared by direct hydrothermal syntheses (NiLTA, CoLTA, FeLTA, NiMFI, CoMFI, FeMFI, NiFAU, CoFAU, FeFAU) and then treated in air at 623–673 K (Section 2.2) are shown in Fig. 1, together with those for metal-free LTA, MFI, and FAU. LTA, MFI, and FAU (Fig. 1) were prepared with 3% wt., 1.5% wt., and 1.5% wt. nominal metal contents, respectively. All samples gave diffraction lines that were sharp and indicative of the exclusive presence of the intended framework. Diffraction features for bulk metal oxides were not detected (e.g., (111) reflection in NiO, 2θ = 37°; (311) in Co_3O_4 2θ = 39°; (311) in Fe_2O_3, 2θ = 36°).

Ni, Co, and Fe contents in the recovered solids were only slightly below those in the synthesis gels (10–20%; Table 2), indicative of the predominant incorporation of the metal precursors into the solids formed and of the ability of alkoxysilane moieties in TPE ligands to promote encapsulation through the formation of siloxane linkages to the nucleating frameworks [8–10]. The remaining ligated precursors were retained within supernatant solutions, which were separated from the solids by filtration (Section 2.2).

The size distributions of oxide nanoparticles after oxidative treatments were measured by transmission electron microscopy (TEM). Surface-averaged particle diameters ($\langle d_{TEM} \rangle$; Eq. (1)), fractional dispersions (D; Eq. (2)), and dispersity indices (DI; Eq. (3)) (Section 2.2) are shown in Table 2 for all samples. TEM data for NiLTA, FeMFI, and CoFAU samples are shown in Fig. 2 and for all other samples (CoLTA, FeLTA, NiMFI, CoMFI, NiFAU, FeFAU) in the SI (Section S5).

Nanoparticles are evident in all zeolite samples, indicative of the removal of the chelating TPE ligands by oxidative treatments and of the nucleation and growth of small nanoparticles (1.5–2.3 nm) uniformly distributed in size (DI < 1.11) during (or after) ligand removal (Table 2). Their mean diameters are slightly larger than the α-cages in LTA (1.1 nm [51]) and FAU (1.1 nm [51]) or than the channel intersections in MFI (0.64 nm [51]), indicative of particle growth that locally disrupts the crystalline frameworks, with the consequent energetic cost of such disruptions likely responsible for limiting particle growth. These framework disruptions cannot be detected in diffractograms (Fig. 1), because the fraction of the crystal volume occupied by oxide particles is less than 1.5% in all samples (calculated from framework densities [51], the number of particles, and the bulk densities of NiO, Co_3O_4, Fe_2O_3). Micropore volume measurements conducted using CO_2 adsorption (Section S6, SI) on metal-LTA (0.32 $cm^3\,g^{-1}$), metal-MFI (0.16–0.17 $cm^3\,g^{-1}$), and metal-FAU (0.34–0.36 $cm^3\,g^{-1}$) samples

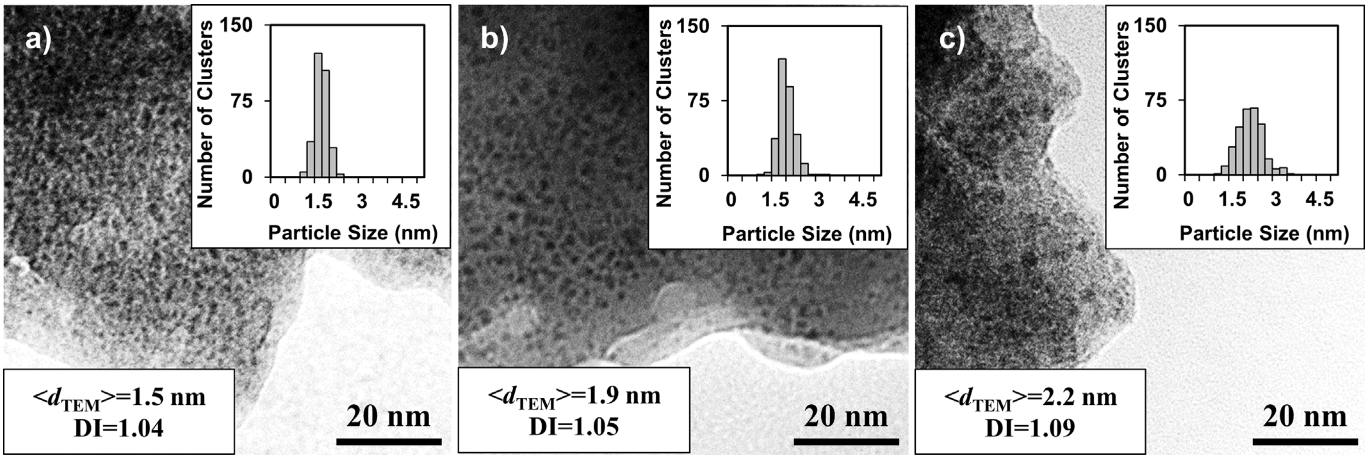

Fig. 2. Electron micrographs, surface-averaged cluster diameters ($< d_{TEM} >$, Eq. (1)), particle dispersity indices (DI, Eq. (3)), and cluster diameter distributions for (a) NiLTA, (b) FeMFI, and (c) CoFAU samples.

were similar to their metal-free counterparts (LTA: 0.34 $cm^3\,g^{-1}$, MFI: 0.19 $cm^3\,g^{-1}$, FAU: 0.38 $cm^3\,g^{-1}$), further confirming that the micropore structures of these zeolites remain largely intact despite the presence of metal oxide nanoparticles within the crystallites. We surmise that the absence of framework disruptions in numbers sufficient to detect their presence by XRD or CO_2 adsorption reflects (i) TPE/T-atom ratios in the synthesis gels (LTA: 0.066–0.071, MFI: 0.021–0.022, FAU: 0.022–0.023) that are well below the critical values that significantly disrupt the assembly of crystalline frameworks (LTA: 0.093–0.11, MFI: 0.044–0.055, FAU: 0.043–0.046; Table 1), (ii) the relatively small fraction of crystal volume occupied by the nanoparticles ultimately formed (< 1.5%), and (iii) partial healing of the framework defects upon oxidative removal of the occluded TPE ligands. Such infrequent disruptions do not compromise the framework integrity or the protection of intracrystalline nanoparticles against sintering or contact with large molecules present in the extracrystalline fluid phase.

Mean diameters were similar for all metals in each given zeolite (e.g., NiLTA: 1.5 ± 0.2 nm, CoLTA: 1.6 ± 0.3 nm, FeLTA: 1.9 ± 0.3 nm); they were smallest in LTA and largest in FAU for a given metal, in spite of the higher metal contents achieved in LTA (2.5–2.7% wt.) than in MFI (1.2–1.3% wt.) or FAU (1.2–1.4% wt.). These trends in size parallel the respective sizes of the apertures in each host framework (LTA: 0.41 nm apertures; 8-MR [51]; 1.5–1.9 nm oxides; MFI: 0.55 nm apertures; 10-MR [51]; 1.7–1.9 nm oxides; FAU: 0.74 nm apertures; 12-MR [51]; 2.2–2.3 nm oxides). These sizes are likely set by kinetic or thermodynamic hurdles to coalescence or sintering, imposed by the confining framework, which must be locally disrupted to allow the growth of nanoparticles [8–10]. The inverse correlation between cluster size and zeolite aperture size may reflect larger energy penalties incurred to rupture smaller apertures.

These data show that oxidative treatments convert ligated precursors into nanoparticles without significant framework disruptions and that TPE ligands prevent the attachment of Ni^{2+}, Co^{2+}, and Fe^{2+} at exchange sites, a process that would have prevented the formation of oxide nanoparticles. Such size and structural stability reflects: (i) the modest temperatures required for ligand removal, (ii) the low density of the oxide nanoparticles that cause the local disruptions, and (iii) the energetic penalties associated with framework disruptions required for nanoparticle growth. The next section confirms that exchanged cations are not detectable by infrared spectra of adsorbed CO and that their reduction rates are consistent with the properties of the oxide nanoparticles that are evident from TEM (Fig. 2), instead of exchanged cations.

3.3. Binding properties and stoichiometry of encapsulated oxide nanoparticles

3.3.1. Infrared spectra of adsorbed CO and evidence for the absence of exchanged metal cations and metal aluminosilicates

Metal oxide particles are generally more effective catalysts [17–23] than isolated exchanged cations [10], because they undergo more facile redox cycles than isolated exchanged cations; these exchanged species are more difficult to reduce [28,30] and exhibit larger HOMO-LUMO gaps than oxide particles [10,56]. The infrared spectra of adsorbed CO show distinct bands for CO coordinated to exchanged cations [57–59] and metal-aluminosilicate compounds [60–62], but much weaker features for CO interacting with oxide nanoparticle surfaces [45–47].

Infrared spectra of CO adsorbed on metal-zeolite samples (273 K; 1 kPa CO) are shown in Fig. 3 for materials prepared by direct hydrothermal synthesis and subsequent oxidative treatments (623–673 K; Section 2.2). The spectra of CO adsorbed onto LTA, MFI, and FAU exchanged with Ni^{2+}, Co^{2+}, or Fe^{2+} (Section 2.2.4) are also shown in Fig. 3. NiLTA, CoLTA, and FeLTA samples were exchanged with Ca^{2+} cations in order to allow the more facile diffusion of CO throughout LTA frameworks (Section 2.2.1).

LTA, MFI, and FAU zeolites exchanged with Ni^{2+}, Co^{2+}, and Fe^{2+} showed intense bands at 2200-2160 cm^{-1}, consistent with carbonyl stretches for CO bound at Ni, Co, and Fe cations [57–59]. Any contributions from CO adsorbed on Na^+ or Ca^{2+} cations were subtracted from these spectra using CO adsorption spectra collected on metal-free LTA, MFI, and FAU (Section 2.3.3). CO absorption bands were much less intense in (metal-exchanged) MFI than for LTA and FAU because of the lower metal contents (LTA, FAU: 2.5–3.0% wt.; MFI: 0.06–0.12% wt.), a consequence, at least in part, of the small number of exchange sites at high Si/Al framework ratios (Section 2.2.4).

Metal-zeolite samples prepared by direct hydrothermal synthesis methods (Section 2.2) did not show detectable infrared bands corresponding to CO coordination at exchanged Ni, Co, or Fe cations (2200-2160 cm^{-1} [57–59]) or at surfaces of metal aluminosilicates (e.g. Ni aluminate, Co silicate, Fe silicate; 2205-2170 cm^{-1} [60–62]). The absence of such features indicates that cations are predominantly present as oxide nanoparticles instead of exchanged species or metal aluminosilicate surfaces. The rates of oxide reduction (Section 3.3.2) and of ethanol oxidation on these oxides (Section 3.4) described below confirm the prevalence of oxide nanoparticles in these samples.

Metal-zeolite samples prepared by direct hydrothermal synthesis did not show detectable bands for CO physisorbed on oxide surfaces (NiO, Co_3O_4, Fe_2O_3) because their weak binding leads to very low surface coverages at 1 kPa CO [45–47]. Such low CO pressures were specifically chosen in order to minimize the concurrent physisorption of

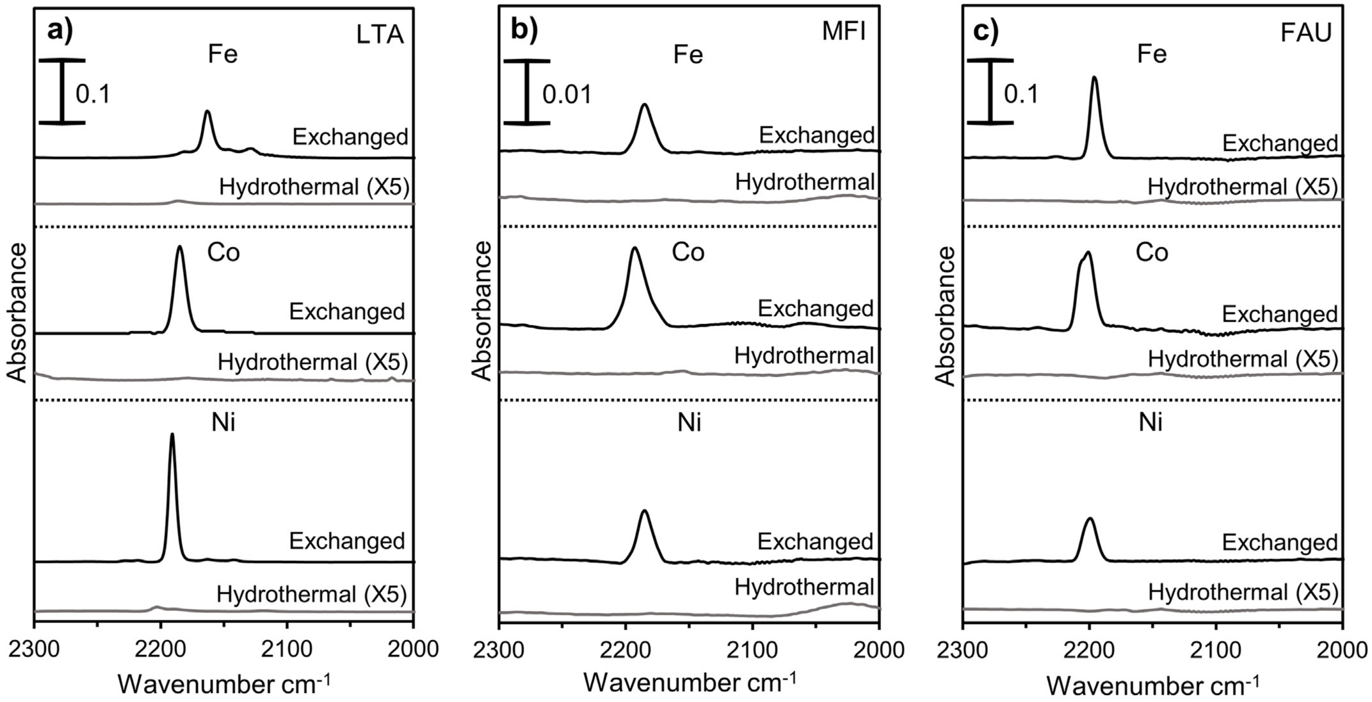

Fig. 3. Infrared difference spectra of CO adsorbed on a) metal-LTA, b) metal-MFI, and c) metal-FAU samples prepared via ion-exchange of metal cations (Ni^{2+}, Co^{2+}, Fe^{2+}; black lines; "exchanged") or by hydrothermal assembly in the presence of ligated metal precursors (gray lines; "hydrothermal"). Spectra were collected on these samples at 273 K (1.0 kPa CO, 99 kPa He) after pretreatment (Section 2.3.3). Spectral contributions of CO(g), CO physisorbed in the frameworks, or CO adsorbed on Na^+ or Ca^{2+} were subtracted (Section 2.3.3).

CO at Na^+ and Ca^{2+} cations [44], which would interfere with infrared features for CO adsorbed onto exchanged Ni^{2+}, Co^{2+}, or Fe^{2+} cations. These results, taken together with TEM data (Fig. 2; Section 3.2.2), show that the ligated precursors confined within all frameworks decompose during oxidative treatments, through the removal of ligands and the formation of oxide nanoparticles; the effects of titration with large organosulfur compounds on ethanol oxidation rates (Section 3.4) show that such nanoparticles reside predominantly within the protected confines of the zeolite voids.

3.3.2. Reduction properties and the stoichiometry of oxide nanoparticles in metal-zeolite samples

The dynamics of reduction, the extent of reduction, and the oxidation states of Ni, Co, and Fe species present in metal-zeolite samples were determined using temperature-programmed reduction (TPR) methods by heating samples from 313 to 1273 K at 0.167 K s^{-1} in flowing 4% H_2/Ar and measuring the amounts of H_2 consumed (Section 2.3.4). The reduction profiles of metal-zeolite samples and of bulk NiO, Co_3O_4, and Fe_2O_3 are shown in Fig. 4. Small oxide domains are more difficult to reduce than larger crystallites because of their more intimate interactions with insulating supports [63] and their larger HOMO-LUMO gaps [56]. Ni, Co, and Fe oxide domains can also form metal aluminates or silicates (e.g., $NiAl_2O_4$, Co_2SiO_4, Fe_2SiO_4 [60–62]) at high temperatures (~800 K or greater) through reactions with aluminosilicates, including in their crystalline zeolite forms [10]. These bulk compounds resist reduction even above 900 K; they can form during TPR before the full reduction of the oxide domains and before or during the incipient thermal degradation of the zeolite frameworks [10,64]. Consequently, these TPR features (Fig. 4) may arise from the reduction of the oxide nanoparticles evident in micrographs (Fig. 2; Section 3.2.2) or from the reduction of metal aluminosilicates that may form in-situ before the full reduction of the oxide nanoparticles.

The reduction of bulk NiO (Fig. 4a) starts at ~530 K and shows the H_2/Ni consumption ratio expected for the reduction of all Ni^{2+} cations to Ni^0 (1.03 vs. 1.0). Ni^{2+} reduces to Ni^0 in a single two-electron reduction event, and the two reduction features for bulk NiO in Fig. 4a reflect bimodal size distributions of NiO crystallites, which lead to concomitant effects of oxide domain size on reduction properties [65]. NiFAU and NiMFI reduce with a single H_2 consumption feature at onset reduction temperatures of 670 K and 690 K, and with H_2/Ni consumption ratios of 1.05 and 1.06, respectively. These data are consistent with the stoichiometry of NiO and with small nanoparticles (1.9–2.3 nm; Table 2) that reduce at higher temperatures than larger bulk NiO crystallites (410 nm; SI, Section S1). NiLTA gave three visible reduction features centered at 730 K (H_2/Ni = 0.17), 930 K (H_2/Ni = 0.66), and 1120 K (H_2/Ni = 0.13), with the onset of reduction at 675 K. The total H_2/Ni consumption ratio (0.96) is consistent with the reduction of all Ni^{2+} species in this sample. The two high-temperature features together account for the majority of the reduced Ni (~82%), and are likely to arise from Ni silicates, which reduce in this temperature range (900–1200 K [66]). Such species, if present after oxidative treatments, would have been evident from their CO infrared bands (Section 3.3.1) given their prevalence in TPR profiles, suggesting that metal aluminosilicates form via reactions between NiO nanoparticles and the LTA frameworks as the latter incipiently degrade before the reduction of NiO is complete. The low-temperature feature (730 K) in NiLTA is typical of small (< 8 nm) NiO crystallites supported on silicates [67] and is likely to arise from reduction of NiO nanoparticles before they form Ni aluminosilicates.

The reduction profiles of bulk Co_3O_4 and of CoFAU, CoMFI, and CoLTA samples are shown in Fig. 4b. Bulk Co_3O_4 reduction becomes detectable at ~500 K and consists of two features (580 K, H_2/Co = 0.33; 680 K, H_2/Co = 1.0), corresponding to the sequential reduction of Co_3O_4 to CoO and then of CoO to Co^0 and consistent with the complete reduction of Co_3O_4 aggregates (H_2/Co = 1.33) [68]. The total H_2/Co consumption ratios for CoFAU, CoMFI, and CoLTA (1.28, 1.21, and 1.16, respectively) are consistent with full reduction of nanoparticles predominantly consisting of Co_3O_4 (H_2/Co = 1.33), but with some particles containing a deficit of Co^{3+} cations. Each sample shows two reduction features (I: 600 K, 710 K, and 920 K; II: 990 K, 1000 K,

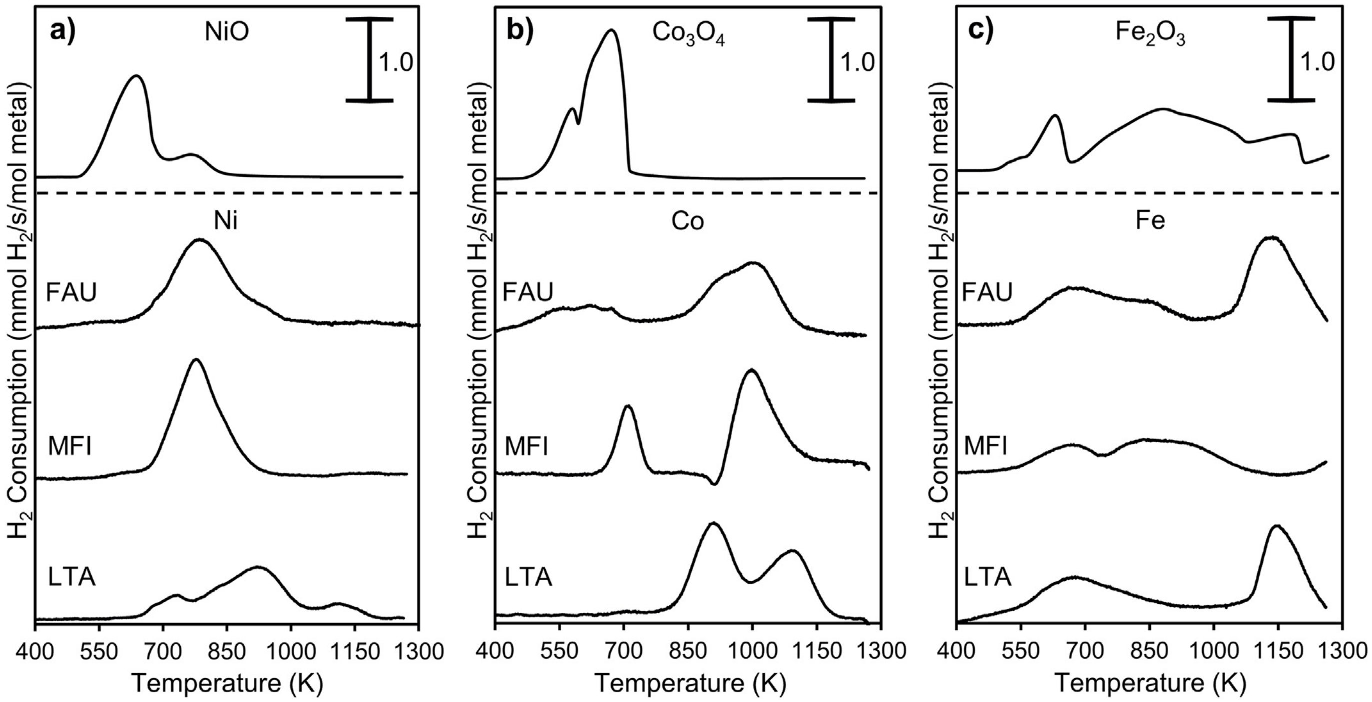

Fig. 4. Temperature programmed reduction profiles of bulk a) Ni, b) Co, and c) Fe oxides and of a) Ni-zeolite, b) Co-zeolite, and c) Fe-zeolite samples prepared via hydrothermal assembly in the presence of ligated metal precursors. Samples were heated in 4% H_2/Ar (8.3 $cm^3\,s^{-1}\,g^{-1}$) from 313 K to 1273 K at 0.167 $K\,s^{-1}$.

and 1100 K; CoFAU, CoMFI, and CoLTA). The high temperature reduction processes occur at temperatures (> 900 K) typical of the reduction of bulk Co_2SiO_4 or $Co_2Al_2O_5$ [69,70], which appear to form before all the Co oxide nanoparticles reduce to Co^0, as in the case of Ni-zeolite samples. Infrared spectra indeed show that treatment of CoLTA at 1020 K in H_2 or O_2 leads to the appearance of CO infrared bands corresponding to these Co aluminosilicates, which occurs after samples are treated at the same temperatures that cause the disappearance of LTA diffraction lines [10].

The first reduction feature in Co-zeolite samples (H_2/Co ratios of 0.35, 0.41, and 0.66 for CoFAU, CoMFI, and CoLTA) is assigned here to the partial reduction of the Co_3O_4 nanoparticles evident in electron micrographs (Fig. 2; Section 3.2.2) to Co metal or CoO. The onset of such reduction features occurs at higher temperatures for CoMFI and CoLTA (660 K, 800 K, respectively) than for bulk Co_3O_4 (~500 K), consistent with their much smaller particle diameters (1.7, 1.6 nm, Table 2 vs. 28 nm, Section S1). The onset of reduction in CoFAU, however, occurs at 530 K, a temperature similar to those required for the incipient reduction of bulk Co_3O_4 (~500 K). The low intensity of this feature (H_2/Co = 0.35) relative to the total H_2 consumed (H_2/Co = 1.28) and its low temperature suggest that it reflects the presence of a few larger Co_3O_4 particles, too few in number to be detectable by TEM (Section 3.2.2) or XRD (Section 3.2.2). Below, reactivity studies and titrations with organosulfur species show that such extrazeolitic clusters constitute a small fraction (< 6%) of the total Co oxide surface area in this sample (Section 3.4). The onset of the second reduction feature in CoFAU (H_2/Co = 0.93) occurs at temperatures (~800 K) similar to those required to reduce the Co_3O_4 nanoparticles in LTA, suggesting that it arises, at least in part, from the reduction of the nanoparticles visible in the electron micrographs of these samples (Fig. 2). This feature is broad and bimodal and extends into the temperature range (810–1150 K) reported for the reduction of Co in aluminosilicates (> 900 K) [69,70], indicative of the partial conversion of Co_3O_4 clusters into Co_2SiO_4 or $Co_2Al_2O_5$ before their complete reduction to Co metal.

The reduction profiles of bulk Fe_2O_3 and of FeFAU, FeMFI, and FeLTA samples derived from direct hydrothermal syntheses are shown in Fig. 4c. Fe_2O_3 reduces in three distinct stages, evident at 630 K (H_2/Fe = 0.17), 700–940 K (H_2/Fe = 0.33), and 900–1200 K (H_2/Fe = 1.0), which correspond to the respective reductions of Fe_2O_3, Fe_3O_4, and FeO [71]. FeFAU and FeLTA each showed two reduction features (I: 730 K and 680 K; II: 1130 K and 1160 K; FeFAU and FeLTA) and gave total H_2/Fe consumption ratios (1.42, 1.43) consistent with the predominant presence of iron(III) oxide (Fe_2O_3; H_2/Fe = 1.5) in these samples after oxidative removal of the ligands from Fe precursors. The high-temperature reduction features in these two samples are attributed to Fe aluminate or silicate species [72,73], which, as in the case of Ni and Co zeolite samples, form via FeO_x reactions with the aluminosilicate frameworks. The first H_2 consumption feature for FeFAU (730 K; H_2/Fe = 0.61) and FeLTA (680 K; H_2/Fe = 0.60) occurs in a temperature range (670–830 K) characteristic of Fe^{3+} to Fe^{2+} reduction in highly-dispersed Fe_2O_3 and Fe_3O_4 on silica [74]. The onset temperatures of reduction for these peaks (~580 K and ~565 K for FeFAU and FeLTA, respectively) are slightly above those required to reduce bulk Fe_2O_3 (~510 K), as expected from the less reducible nature of small oxide domains. The H_2/Fe ratios for these low-temperature features in the reduction profiles of FeFAU (H_2/Fe = 0.61) and FeLTA (H_2/Fe = 0.60) are similar to those expected from the reduction of Fe^{3+} in Fe_2O_3 to Fe^{2+} ($Fe_2O_3 \rightarrow FeO$; H_2/Fe = 0.5), indicating that Fe aluminosilicate species, which are responsible for the second reduction feature (FeFAU: 1130 K, H_2/Fe = 0.81; FeLTA: 1160 K, H_2/Fe = 0.83), are derived from FeO nanoparticles formed via Fe^{3+} reduction in Fe_2O_3.

FeMFI reduced in two stages (675 K (H_2/Fe = 0.29); 875 K (H_2/Fe = 0.64)). The onset temperature for the first feature (~550 K) is slightly higher than for bulk Fe_2O_3 (~510 K), as expected from the small Fe_2O_3 domains present within FeMFI. These two H_2 consumption features appear to reflect, as is the case for bulk Fe_2O_3, the sequential reduction of trivalent Fe via the conversion of Fe_2O_3 to Fe_3O_4 and then Fe_3O_4 to FeO, respectively. H_2/Fe ratios of these reduction features, however, were greater than would be expected for the exclusive reduction of trivalent Fe within Fe_2O_3 (H_2/Fe = 0.5) via a two-step process (I: $Fe_3O_4 \rightarrow Fe_2O_3$, H_2/Fe = 0.17; II: $Fe_2O_3 \rightarrow FeO$, H_2/Fe = 0.33), indicating that a portion of the H_2 consumed accounts for the reduction of divalent FeO in tandem with the reduction of Fe_2O_3

and Fe_3O_4. The total H_2/Fe consumption ratio (0.93) is significantly lower than that expected for the total reduction of Fe_2O_3 (1.5) to Fe^0, consistent with the presence of unreactive Fe silicates [73] or aluminates [72] that form during thermal treatment in H_2 and which could not be reduced even at 1270 K.

These data, taken together with results from TEM (Section 3.2.2) and infrared spectra (Section 3.3.1), indicate the predominant presence of well-dispersed base metal oxides within zeolite void structures and with the stoichiometry of NiO, Co_3O_4, and Fe_2O_3. Their small sizes are evident from their resistance to reduction in comparison with bulk oxides and are generally consistent with TEM-derived size distributions. Their reduction temperatures can lead to the incorporation of cations into aluminosilicate compounds, within which such cations become even more resistant to reduction. The mean diameters of the oxide domains (1.5–2.3 nm) are slightly larger than the void diameters of LTA (1.1 nm [51]), MFI (0.64 nm [51]), and FAU (1.1 nm [51]); the resulting framework disruptions may lead to local defects near the oxide domains, which would favor the formation of metal aluminosilicates. Such metal aluminosilicates may form in tandem with, and as a result of, the incipient structural collapse of the crystalline frameworks, which occurs at temperatures [LTA (~1000 K) [75], MFI (~1300 K) [76], or FAU (~1160 K) [77]] slightly above those required to form these refractory compounds, as previously proposed for Co oxides within LTA [10]. In the next section, we demonstrate that the oxide nanoparticles evident from TEM data are redox active and that they reside within regions inaccessible to large organosulfur titrants, as expected from their predominant presence within zeolite crystals.

3.4. Encapsulation selectivities from ethanol oxidation rates with and without titration of extracrystalline oxide surfaces by large organosulfur compounds

Nanoparticles encapsulated within microporous zeolites benefit from the molecular sieving and size-selective effects conferred by the small apertures within the host void structures. Such effects include the protection of nanoparticle active surfaces from contact with large reactant or poison molecules [8], the resistance against coalescence with adjacent particles [9], and the stabilization of specific transition states by the confining framework [7]. These effects are dictated, in all cases, by the size of the voids and of their connecting apertures within a given zeolite and by the corresponding dimensions of the molecules, intermediates, and transition states involved [8].

The size-selective properties of zeolites are exploited here in assessing the selectivity of metal encapsulation through measurements of ethanol (EtOH) oxidation rates on samples exposed to a bulky organosulfur titrant (2,4,6-trimethylbenzyl mercaptan; TMBM). Thiols such as dodecanethiol and TMBM form thiolates via reactions with Ni, Co, or Fe oxide surfaces [78]; these bound species block active surfaces and thus suppress the rates of catalytic reactions. EtOH (0.40 nm kinetic diameter [79]) diffuses readily through the apertures in LTA (0.41 nm [51]), MFI (0.55 nm [51]), and FAU (0.74 nm [51]), but TMBM (kinetic diameter > 0.86 nm [80]) is essentially excluded from intracrystalline regions. As a result, EtOH oxidation turnover rates on bulk oxides (NiO, Co_3O_4, Fe_2O_3) and on oxide domains at external zeolite crystal surfaces would be suppressed by exposure to TMBM, but turnovers occurring on domains present within LTA, MFI, and FAU crystals would remain active. The effects of TMBM exposure on ethanol oxidation rates thus reflect the fraction of the oxide surfaces that reside within the protected environment of zeolite crystals.

EtOH oxidation rates were measured on bulk NiO, Co_3O_4, Fe_2O_3, and metal-zeolite samples at 393 K before and after ex-situ exposure to TMBM using the procedures described in Section 2.3.5. An inhibition factor (λ) is defined here as the ratio of the rates measured on samples with exposure ($r_{i,j,s}$) and without exposure ($r_{i,j}$) to TMBM titrants:

$$\lambda_{i,j} = \frac{r_{i,j,s}}{r_{i,j}} \tag{4}$$

where the subscript i denotes the metal (Ni, Co, Fe) and j either the bulk metal oxide (b) or the specific zeolite framework (LTA, MFI, or FAU). The magnitude of $\lambda_{i,b}$ for bulk oxides reflects the residual reactivity and in turn the fraction of active surface area that remains untitrated by TMBM, with $\lambda_{i,b}$ values of zero indicative of full suppression of rates and unity an indication of surfaces that do not interact with TMBM strongly enough to prevent ethanol oxidation turnovers.

On bulk NiO, Co_3O_4, and Fe_2O_3, the prevalence of mesopores allows EtOH and TMBM to access catalytic surfaces without diffusional hindrance. Consequently, their $\lambda_{i,b}$ values reflect the accessibility and reactivity of such surfaces after interactions with TMBM. The apertures in zeolites, by contrast, protect intracrystalline oxide domains from contact with TMBM titrants, but allow EtOH and O_2 reactants to access intracrystalline regions. In such samples, only the oxide domains present at the external surfaces of zeolite crystals are titrated by TMBM. Their $\lambda_{i,j}$ values therefore reflect the fraction of the catalytic surface area that resides within the protected confines of zeolite crystals ($F_{i,j}$). These $\lambda_{i,j}$ values, however, are not strictly proportional to $F_{i,j}$ because bulk oxides (and thus clusters present outside zeolite crystals) may retain some reactivity even after extended contact with TMBM. These effects require that we account for the residual reactivity of the titrated oxide surfaces after exposure to TMBM in order to determine $F_{i,j}$:

$$F_{i,j} = \lambda_{i,j} - \lambda_{i,b}\frac{(1-\lambda_{i,j})}{(1-\lambda_{i,b})} \tag{5}$$

Equation (5) corrects $\lambda_{i,j}$ in order to accurately reflect $F_{i,j}$ values by subtracting contributions to $\lambda_{i,j}$ derived from residual rates on TMBM-titrated surfaces (the second term in Eq. (5)). In addition, extrazeolitic oxide surfaces are exposed to the reactant concentrations prevalent in the extracrystalline gas phase (4 kPa EtOH, 9 kPa O_2; Section 2.3.5), but concentration gradients within zeolite crystals would lead to lower oxidation turnover rates on encapsulated oxide surfaces than on those at external surfaces or bulk oxides. These diffusional effects lead to $\lambda_{i,j}$ (and $F_{i,j}$) values that underestimate the actual encapsulation selectivity. These $F_{i,j}$ values also ignore the slow but finite diffusion rates of TMBM through FAU apertures, which would titrate some intracrystalline oxide surfaces and cause $F_{i,j}$ values to be lower than the actual encapsulation selectivity. Consequently, these $F_{i,j}$ values represent a conservative lower limit for the preference of oxide nanoparticles to reside within intracrystalline locations as a result of the synthetic protocols reported in this study.

The $\lambda_{i,j}$ and $F_{i,j}$ values derived from EtOH oxidation rates before and after titration of unprotected surfaces are shown in Table 3. EtOH oxidation turnover rates for each given metal increased monotonically with the size of the framework aperture (LTA: 0.41 nm, MFI: 0.55 nm, FAU: 0.74 nm [51]) for untitrated samples, consistent with diffusional constraints that cause intracrystalline concentration gradients and lower reaction rates. The presence of such diffusional constraints provides independent de facto evidence that these oxide nanoparticles reside predominantly within zeolite crystals. Turnover rates on bulk oxides were higher than on metal-zeolite samples, because of the lack of diffusional constraints and the higher redox surface reactivity typical of larger oxide domains [10,56]. Co_3O_4 (28 nm aggregates, Section S1) gave the highest turnover rate (0.68 mmol s^{-1}) among the three bulk oxides (NiO: 0.25 mmol s^{-1}, 410 nm; Fe_2O_3: 0.12 mmol s^{-1}, 76 nm), reflecting the greater intrinsic redox activity of the Co cations within Co oxide relative to Ni and Fe oxides. Co^{2+} cations exchanged within LTA, MFI, and FAU zeolites (Section 2.2.4), however, did not oxidize EtOH at detectable rates (< 0.00001 mmol s^{-1}) as the bulk (0.68 mmol s^{-1}) or zeolite-encapsulated Co oxides (0.0062–0.10 mmol s^{-1}; Table 3) did, a consequence of exchanged Co^{2+} cations that are much less reducible than bulk oxides or oxide nanoparticles (TPR data in Section S7, SI).

Encapsulation selectivities were > 0.93 for all metal-zeolite samples

Table 3
Ethanol oxidation turnover rates and encapsulation selectivities of metal-zeolite and bulk metal oxide samples.

Sample	r (10^{-3} s^{-1} $mol_{surf\text{-}metal}^{-1}$)[a]	Inhibition Factor (λ)[b]	Encapsulation Selectivity (F)[c]
NiLTA	0.0030	0.99	0.99
NiMFI	0.030	0.96	0.96
NiFAU	0.046	0.93	0.93
CoLTA	0.0062	0.98	0.97
CoMFI	0.061	0.96	0.96
CoFAU	0.10	0.95	0.94
FeLTA	0.0071	0.99	0.97
FeMFI	0.025	0.98	0.93
FeFAU	0.033	0.71	0.12
NiO	0.25	0.12	0
Co_3O_4	0.68	0.12	0
Fe_2O_3	0.12	0.67	0

[a] EtOH oxidation turnover rates of samples suspended in liquid EtOH (300 cm^3 g^{-1}) at ambient temperature for 2 h (for Ni, Co samples) or 16 h (for Fe samples) and then used in reaction (9 kPa O_2, 4 kPa EtOH) at 393 K. Turnover rates are defined as the moles of EtOH converted per unit time normalized by the number of exposed metal surface atoms estimated from particle dispersions or BET surface areas (Section 2.3.5).

[b] r_S/r (Eq. (4)), where r_S are EtOH oxidation rates measured on similarly treated samples but with TMBM dissolved in the EtOH to achieve a 0.2 M solution.

[c] Encapsulation selectivity, defined as the fraction of active metal oxide surface area encapsulated within zeolite crystallites, as estimated from λ values (Eq. (5)).

(except FeFAU; $F_{Fe,FAU} = 0.12$), indicating that the oxide nanoparticles evident in electron micrographs (Section 3.2.2) reside predominantly within zeolite crystallites. The FeFAU data reflects the gradual diffusion of TMBM within FAU over the time required to titrate Fe oxide surfaces. Fe_2O_3, FeLTA, FeMFI, and FeFAU were exposed to TMBM for longer times (16 h; Section 2.3.5) than the Ni or Co samples (2 h), because longer times were required to significantly suppress of rates on bulk Fe_2O_3 ($\lambda_{Fe,b} = 0.67$). Rates were more strongly suppressed by TMBM titration on NiO ($\lambda_{Ni,b} = 0.12$) and Co_3O_4 ($\lambda_{Co,b} = 0.12$), even after shorter exposure times (2 h), and were essentially constant with longer TMBM exposure times (16 h; $\lambda_{Ni,b} = 0.10$; $\lambda_{Co,b} = 0.08$). Treatment of NiFAU and CoFAU with TMBM for 16 h, however, leads to more severe suppression of rates ($\lambda_{Ni,FAU} = 0.47$; $\lambda_{Co,FAU} = 0.52$) than 2 h treatment ($\lambda_{Ni,FAU} = 0.93$; $\lambda_{Co,FAU} = 0.95$). These effects of TMBM exposure times on NiFAU and CoFAU (but not for their LTA or MFI counterparts) indicate that TMBM gradually enters large-pore zeolites and titrates intracrystalline oxide surfaces. As a result, the value of $F_{Fe,FAU}$ reported in Table 3 (0.12), which required longer exposures because of the kinetic hurdles for TMBM binding on Fe oxides, does not accurately reflect its encapsulation selectivity. Its true encapsulation selectivity is likely to resemble that shown by all other samples, for which $F_{i,j}$ values more accurately reflect such selectivities.

These results, taken together, show how synthetic hurdles that impede the selective encapsulation of base metals within microporous voids can be systematically addressed and overcome through general strategies that lead to encapsulation for a broad range of zeolite frameworks. Encapsulation of NiO, Co_3O_4, and Fe_2O_3 clusters was achieved in LTA, MFI, and FAU frameworks, materials that differ substantially in their Si/Al ratios (1.0, 30, 2.3), aperture sizes (8-MR, 0.41 nm; 10-MR, 0.55 nm; 12-MR, 0.74 nm), and in the conditions required for their crystallization (Section 2.2). For all metal species and frameworks, bifunctional TPE ligands successfully stabilize metal precursors against precipitation in synthesis gels, enforce their uptake into zeolite crystals, and are removed by oxidative treatments without damage to the host framework. These synthesis procedures and post-synthetic oxidative treatments lead to the aggregation of small and nearly monodisperse oxide nanoparticles that reside predominantly within zeolite crystals and which do not form redox-inactive metal aluminosilicates or exchanged cations. These high encapsulation selectivities are the result of the chelating properties of the bidentate amine moiety in TPE ligands, which prevent cation precipitation during synthesis and the attachment of metal cations to zeolite exchange sites; they also reflect the role of the ligand alkoxysilane moieties, which bind ligated precursors to nucleating zeolite structures through the formation of covalent siloxane linkages. The broad success of these protocols bodes well for their extension to other zeolite frameworks and metal species, and to the preparation of multimetallic clusters by combining ligated precursors of two or more metals.

4. Conclusions

Ni, Co, and Fe oxide nanoparticles were selectively encapsulated within LTA, MFI, and FAU zeolites using a generalized synthetic procedure. Encapsulation was achieved in all cases through the analogous incorporation of metal cation precursors (Ni^{2+}, Co^{2+}, Fe^{2+}) protected by chelating ligands (N-[3-(trimethoxysilyl)propyl]ethylenediamine) into zeolite synthesis gels, which were allowed to crystallize under hydrothermal conditions to form zeolites with occluded ligated metal species. The ligands preclude premature precipitation of the metal cation precursors as bulk oxide or hydroxide aggregates under the alkaline conditions required for framework assembly, and form covalent linkages with nucleating zeolites to promote metal uptake into the crystallized frameworks. Treatment of these frameworks under oxidative conditions leads to the formation of highly dispersed (< 2.5 nm) metal oxide nanoparticles that are homogeneous in size. Characterization of these materials with infrared spectroscopy indicated the absence of base metal species in the form of exchanged cations or metal aluminosilicates, consistent with the selective formation of metal oxide nanoparticles during oxidative treatment. The reducibility of the base metal species in H_2 and the stoichiometry of their reduction were consistent with the presence of small NiO, Co_3O_4, or Fe_2O_3 clusters. The overwhelming majority of active metal oxide surfaces (> 92%) were protected from contact by large organosulfur poison molecules that selectively or exclusively titrate extrazeolitic metal oxide clusters, confirming that the nanoparticles formed by the synthesis technique predominantly reside within zeolite crystals. This work presents a generalized synthesis technique for encapsulating base metal oxides within zeolites, and demonstrates the efficacy of the technique through its successful application to a variety of metal species (Ni, Co, Fe) and zeolite frameworks (LTA, MFI, FAU). The synthetic approach shown here also illustrates guiding principles and strategies that can be applied to prepare an even wider variety of zeolite-encapsulated base metal clusters. Such materials have potential catalytic applications that seek to combine the catalytic chemistries of metal oxide surfaces with the molecular size and shape selectivity, transition state selectivity, and thermal stability conferred by encapsulation within zeolites.

Notes

The authors declare the following competing financial interest(s): (1) The funding for the research came from Chevron Energy Technology Co. and (2) Stacey I. Zones is an employee of this company and, more generally, is also a stockholder in Chevron Corp.

Acknowledgements

We gratefully acknowledge the Chevron Energy Technology Co for their generous financial support of this research, as well as ancillary support provided for TO by an ARCS foundation fellowship and a National Science Foundation fellowship.

Appendix A. Supplementary data

Supplementary data related to this article can be found at http://dx.doi.org/10.1016/j.micromeso.2018.04.045.

References

[1] R.T. Pabalan, F.P. Bertetti, Rev. Mineral. Geochem. 45 (2001) 453–518.
[2] M. Noack, J. Caro, Microporous Mesoporous Mater. 115 (2008) 215–233.
[3] B.M. Weckhuysen, J. Yu, Chem. Soc. Rev. 44 (2015) 7022–7024.
[4] T. Ennaert, J. Van Aelst, J. Dijkmans, R. De Clercq, W. Schutyser, M. Dusselier, D. Verboekend, B.F. Sels, Chem. Soc. Rev. 45 (2016) 584–611.
[5] J.D. Rimer, M. Kumar, R. Li, A.I. Lupulescu, M.D. Oleksiak, Catal. Sci. Technol. 4 (2014) 3762–3771.
[6] M.A. Deimund, L. Harrison, J.D. Lunn, Y. Liu, A. Malek, R. Shayib, M.E. Davis, ACS Catal. 6 (2016) 542–550.
[7] B. Song, A.-Y. Lo, J. Wang, Mol. Catal. 437 (2017) 47–56.
[8] T. Otto, S.I. Zones, E. Iglesia, J. Catal. 339 (2016) 195–208.
[9] T. Otto, J.M. Ramallo-López, L.J. Giovanetti, F.G. Requejo, S.I. Zones, E. Iglesia, J. Catal. 342 (2016) 125–137.
[10] T. Otto, S.I. Zones, Y. Hong, E. Iglesia, J. Catal. 356 (2017) 173–185.
[11] Z. Wu, S. Goel, M. Choi, E. Iglesia, J. Catal. 311 (2014) 458–468.
[12] S.J. Cho, R. Ryoo, J. Phys. Chem. B 105 (2001) 1293–1298.
[13] M. Moliner, J.E. Gabay, C.E. Kliewer, R.T. Carr, J. Guzman, G.L. Casty, P. Serna, A. Corma, J. Am. Chem. Soc. 138 (2016) 15743–15750.
[14] K.T. Højholt, A.B. Laursen, S. Kegnæs, C.H. Christensen, Top. Catal. 54 (2011) 1026–1033.
[15] V. Sebastian, S. Irusta, R. Mallada, J. Santamaría, Appl. Catal., A 366 (2009) 242–251.
[16] L. Djakovitch, K. Koehler, J. Am. Chem. Soc. 123 (2001) 5990–5999.
[17] J.J. Foster, R.I. Masel, Ind. Eng. Chem. Prod. Res. Dev. 25 (1986) 563–568.
[18] V. Iablokov, R. Barbosa, G. Pollefeyt, I. Van Driessche, S. Chenakin, N. Kruse, ACS Catal. 5 (2015) 5714–5718.
[19] A.K. Kandalam, B. Chatterjee, S.N. Khanna, B.K. Rao, P. Jena, B.V. Reddy, Surf. Sci. 601 (2007) 4873–4880.
[20] M. Shamsipur, M. Najafi, M.-R. Milani Hosseini, J. Appl. Electrochem. 43 (2013) 1027–1033.
[21] J. Zhu, K. Kailasam, A. Fischer, A. Thomas, ACS Catal. 1 (2011) 342–347.
[22] C. González-Arellano, J.M. Campelo, D.J. Macquarrie, J.M. Marinas, A.A. Romero, R. Luque, ChemSusChem 1 (2008) 746–750.
[23] S. Bhavsar, G. Veser, Energy Fuels 27 (2013) 2073–2084.
[24] J. Sehested, Catal. Today 111 (2006) 103–110.
[25] H. Adkins, H.I. Cramer, J. Am. Chem. Soc. 52 (1930) 4349–4358.
[26] H. Schulz, Stud. Surf. Sci. Catal. 163 (2007) 177–199.
[27] B. Wilk, R. Pelka, W. Arabczyk, J. Phys. Chem. C 121 (2017) 8548–8556.
[28] E. Asedegbega-Nieto, E. Díaz, A. Vega, S. Ordóñez, Catal. Today 157 (2010) 425–431.
[29] A. Borqschulte, E. Callini, N. Stadie, Y. Arroyo, M.D. Rossell, R. Erni, H. Geerlings, A. Züttel, D. Ferri, Catal. Sci. Technol. 5 (2015) 4613–4621.
[30] Y. Wang, H. Wu, Q. Zhang, Q. Tang, Microporous Mesoporous Mater. 86 (2005) 38–49.
[31] D. Fraenkel, B.C. Gates, J. Am. Chem. Soc. 102 (1980) 2478–2480.
[32] H. Inokawa, M. Maeda, S. Nishimoto, Y. Kameshima, M. Miyake, T. Ichikawa, Y. Kojima, H. Miyaoka, Int. J. Hydrogen Energy 38 (2013) 13579–13586.
[33] J. Liu, D. Wang, J.-F. Chen, Y. Zhang, Int. J. Hydrogen Energy 41 (2016) 21965–21978.
[34] L. Luo, C. Dai, A. Zhang, J. Wang, M. Liu, C. Song, X. Guo, RSC Adv. 5 (2015) 29509–29512.
[35] B. Gevert, L. Eriksson, A. Törncrona, J. Porous Mater. 18 (2011) 723–728.
[36] Z. Liu, C. Shi, D. Wu, S. He, B. Ren, J. Nanotechnol. 2016 (2016) 1–6.
[37] W. Li, S.Y. Yu, G.D. Meitzner, E. Iglesia, J. Phys. Chem. B 105 (2001) 1176–1184.
[38] R.P. Townsend, E.N. Coker, H. van Bekkum, E.M. Flanigen, P.A. Jacobs, J.C. Jansen (Eds.), Studies in Surface Science and Catalysis, second ed., Elsevier Science B.V., Amsterdam, 2001, p. 512.
[39] C.M. de Correa, A.L. Villa, M. Zapata, Catal. Lett. 38 (1996) 27–32.
[40] G. Bergeret, P. Gallezot, G. Ertl, H. Knozinger, F. Schuth, J. Weitkamp (Eds.), Handbook of Heterogeneous Catalysis, second ed., Wiley-VHC, Weinheim, 2008, pp. 738–765.
[41] A. Leineweber, H. Jacobs, S. Hull, Inorg. Chem. 40 (2001) 5818–5822.
[42] I.S. Kotousova, S.M. Polyakov, Kristallografiya 17 (1972) 661–663.
[43] N. Dzade, A. Roldan Martinez, N. de Leeuw, Minerals 4 (2014) 89–115.
[44] T. Montanari, I. Salla, G. Busca, Microporous Mesoporous Mater. 109 (2008) 216–222.
[45] E.E. Platero, D. Scarano, G. Spoto, A. Zecchina, Faraday Discuss. Chem. Soc. 80 (1985) 183–193.
[46] H.-K. Lin, C.-B. Wang, H.-C. Chiu, S.-H. Chien, Catal. Lett. 86 (2003) 63–68.
[47] A. Zecchina, D. Scarano, A. Reller, J. Chem. Soc., Faraday Trans. 1 84 (1988) 2327–2333.
[48] M. Ul-Haque, C.N. Caughlan, K. Emerson, Inorg. Chem. 9 (1970) 2421–2424.
[49] K. Cooke, A.V. Olenev, K. Kovnir, Acta Crystallogr. E 69 (2013) m332.
[50] T.J. Smith, J. Mol. Graph. 13 (1995) 122–125.
[51] C.M. Baerlocher, Database of zeolite structures, accessed February 2018, 2017. http://www.iza-structure.org/databases/, .
[52] K. Miyake, Y. Hirota, K. Ono, Y. Uchida, M. Miyamoto, N. Nishiyama, New J. Chem. 41 (2017) 2235–2240.
[53] P. Ratnasamy, R. Kumar, Catal. Today 9 (1991) 329–416.
[54] J.W. Steed, J.L. Atwood, Supramolecular Chemistry, second ed., Wiley, Chichester, 2009, pp. 106–219.
[55] T. Chatelain, J. Patarin, M. Soulard, J.L. Guth, P. Schulz, Zeolites 15 (1995) 90–96.
[56] D.G. Barton, M. Shtein, R.D. Wilson, S.L. Soled, E. Iglesia, J. Phys. Chem. B 103 (1999) 630–640.
[57] C.L. Angell, P.C. Schaffer, J. Phys. Chem. 70 (1966) 1413–1417.
[58] V. Rakić, V. Dondur, R. Hercigonja, J. Serb. Chem. Soc. 68 (2003) 409–416.
[59] J. Kim, A. Jentys, S.M. Maier, J.A. Lercher, J. Phys. Chem. C 117 (2013) 986–993.
[60] C.O. Areán, M.P. Mentruit, A.J. López López, J.B. Parra, Colloids Surf., A 180 (2001) 253–258.
[61] V. Subramanian, V.L. Zholobenko, K. Cheng, C. Lancelot, S. Heyte, J. Thuriot, S. Paul, V.V. Ordomsky, A.Y. Khodakov, ChemCatChem 8 (2016) 380–389.
[62] A.F.H. Wielers, A.J.H.M. Kock, C.E.C.A. Hop, J.W. Geus, A.M. van Der Kraan, J. Catal. 117 (1989) 1–18.
[63] J.-C. Kim, S. Lee, K. Cho, K. Na, C. Lee, R. Ryoo, ACS Catal. 4 (2014) 3919–3927.
[64] J. Zieliński, J. Chem. Soc., Faraday Trans. 93 (1997) 3577–3580.
[65] J. Sá, Y. Kayser, C.J. Milne, D.L.A. Fernandes, J. Szlachetko, Phys. Chem. Chem. Phys. 16 (2014) 7692–7696.
[66] Z. Zhao, N. Lakshminarayanan, S.L. Swartz, G.B. Arkenberg, L.G. Felix, R.B. Slimane, C.C. Choi, U.S. Ozkan, Appl. Catal., A 489 (2015) 42–50.
[67] B. Solsona, P. Concepción, J.M. López Nieto, A. Dejoz, J.A. Cecilia, S. Agouram, M.D. Soriano, V. Torres, J. Jiménez-Jiménez, E.R. Castellón, Catal. Sci. Technol. 6 (2016) 3419–3429.
[68] A. Kogelbauer, J.C. Weber, J.G. Goodwin Jr., Catal. Lett. 34 (1995) 259–267.
[69] Y. Okamoto, K. Nagata, T. Adachi, T. Imanaka, K. Inamura, T. Takyu, J. Phys. Chem. 95 (1991) 310–319.
[70] D.J. Moodley, A.M. Saib, J. van de Loosdrecht, C.A. Welker-Nieuwoudt, B.H. Sigwebela, J.W. Niemantsverdriet, Catal. Today 171 (2011) 192–200.
[71] Z. Liu, H. Su, B. Chen, J. Li, S.I. Woo, Chem. Eng. J. 299 (2016) 255–262.
[72] J.C. Acomb, C. Wu, P.T. Williams, Appl. Catal., B 180 (2016) 497–510.
[73] C.-H. Zhang, H.-J. Wan, Y. Yang, H.-W. Xiang, Y.-W. Li, Catal. Commun. 7 (2006) 733–738.
[74] C. Messi, P. Carniti, A. Gervasini, J. Therm. Anal. Calorim. 91 (2008) 93–100.
[75] S. Bhatia, Zeolite Catalysis: Principles and Applications, CRC Press, Inc., Boca Raton, 1990, p. 10.
[76] J.L. Tallon, R.G. Buckley, J. Phys. Chem. 91 (1987) 1469–1475.
[77] W.J. Ambs, W.H. Flank, J. Catal. 14 (1969) 118–125.
[78] P.G. Hoertz, J.R. Niskala, P. Dai, H.T. Black, W. You, J. Am. Chem. Soc. 130 (2008) 9763–9772.
[79] R.L. Van Mao, T.M. Nguyen, G.P. Mclaughlin, Appl. Catal. 48 (1989) 265–277.
[80] N.M. Tukur, S. Al-Khattaf, Energy Fuels 21 (2007) 2499–2508.